LUNDS UNIVERSITET
Lunds Tekniska Högskola

Heat Transfer Investigations by Liquid Crystal Thermography in Gas Turbine Related Applications

Chenglong Wang

Thesis for the degree of Licentiate of Engineering, 2014

Division of Heat Transfer
Department of Energy Sciences
Faculty of Engineering (LTH)
Lund University

www.energy.lth.se

Abstract

Heat transfer in gas turbine related applications is investigated by the liquid crystal thermography (LCT). The work presented in this thesis can be divided into two parts.

In the first part, heat transfer measurements on an outlet guide vane (OGV) and the endwall are carried out in a linear cascade. Because the OGV has a complex curved surface, it is necessary to calibrate the LCT by taking into account the effect of viewing angles of the camera. Based on the calibration results, heat transfer measurements on the OGV and the endwall were conducted. Both on- and off-design conditions were tested, where the incidence angles of the OGV were +25 and -25 degrees, respectively. In addition, heat transfer on the endwall of the OGV with +40 degrees incidence angle was measured. The results indicate that the incidence angles have considerable influences upon the heat transfer on both the OGV and endwall surfaces. For on-design conditions, laminar-turbulent boundary layer transitions occur on both sides of the OGV, but no flow separation occurs on the OGV or the endwall. On the contrary, for off-design conditions, the position of laminar-turbulent boundary layer transition on the OGV is significantly displaced downstream on the suction surface, and a separation region occurs from the leading edge on the pressure side of the OGV and the endwall. As expected, a larger Reynolds number gives higher heat transfer coefficients on both sides of the OGV.

In the second part, an experimental investigation of heat transfer and pressure drop in the turn region of a U-bend channel has been carried out. The LCT method is used to obtain detailed heat transfer distributions. Eight cases were tested, including one smooth, and seven different ribbed turn surfaces. Results indicate that heat transfer on the smooth outer wall is dominated by the flow impingement. When ribs are fitted onto the outer wall, it is found that the heat transfer patterns are significantly altered. The presence of ribs augments the heat transfer at the penalty of increased pressure loss. Thermal performance and heat transfer non-uniformity are considered to provide optimized rib configurations.

Keywords: heat transfer, gas turbine, liquid crystal thermography, outlet guide vane, blade tip cooling.

Acknowledgments

List of publications

1. **Chenglong Wang**, Lei Wang, Bengt Sundén, Valery Chernoray, and Hans Abrahamsson, 2014, "An Experimental Study of Heat Transfer on An Outlet Guide Vane", Proceedings of ASME Turbo Expo 2014, June 16-20, Düsseldorf, Germany, GT2014-25100.

2. **Chenglong Wang**, Lei Wang and Bengt Sundén, 2014, "An Experimental Study of Heat Transfer in the Turn Region of a U-bend Channel with Various Ribs", Proceedings of the 15th International Heat Transfer Conference, August 10-15, Kyoto, Japan, IHTC15-8864.

3. Lei Wang, Zahra Ghorbani-Tari, **Chenglong Wang**, Zan Wu, and Bengt Sundén, 2013, "Endwall Heat Transfer at the Turn Section in a Two-pass Square Channel with and without Ribs", Journal of Enhanced Heat Transfer, 20(4), pp: 321-332.

Nomenclature

A	heating surface area [m^2]
C_p	pressure coefficient on the OGV [-]
D_h	hydraulic diameter of the U-bend channel [m]
e	rib height [m]
f	Darcy friction factor in the U-bend channel [-]
f_0	Darcy friction factor in a smooth straight channel [-]
h	convective heat transfer coefficient [W m^{-2} K^{-1}]
k	thermal conductivity of air [W m^{-1} K^{-1}]
H	distance between inner and outer wall [m]
K	non-dimensionalized pressure drop in the U-bend channel [-]
L	OGV axial chord length [m]
m	mass flow rate in the U-bend channel [kg s^{-1}]
N	total number of measuring points [-]
Nu	Nusselt number [-]
Nu_i	Nusselt number at point i [-]
$\overline{Nu}$	total averaged Nusselt number [-]
Nu_0	Nusselt number in a smooth straight channel [-]
$(Nu/Nu_0)_{std}$	standard deviation of normalized Nusselt number distributions [-]
p	rib pitch [m]
P_s	static pressure on the vane [Pa]
$P_{s,in}$	static pressure of the inlet flow [Pa]
$P_{dyn,in}$	dynamic pressure of the inlet flow [Pa]
Pr	Prandtl number of air [-]
q_w	heat flux [W m^{-2}]
q_{loss}	heat flux loss on the wall [W m^{-2}]
Re	Reynolds number [-]
T_w	wall temperature [K]
T_0	air bulk temperature [K]
T_{in}	inlet air temperature [K]
T_{out}	outlet air temperature [K]

U_0	axial velocity [m s^{-1}]
W_{out}	the outer wall length [m]
W_{in}	the inner wall length [m]
X	streamwise direction [-]
Y	spanwise direction [-]
Z	normal direction [-]

Greek symbols

Δp	pressure drop [Pa]
v	kinematic viscosity of air [m^2 s^{-1}]
ρ	density of air [kg m^{-3}]
η	thermal performance [-]

Contents

1 Introduction

Gas turbines are widely used in aircraft propulsion, land-based power generation and many other industrial applications. Modern development in gas turbine heat transfer and cooling technique plays a critical role in increasing the thermal efficiency and power output of advanced gas turbines [1].

This work consists of two parts, regarding the heat transfer of an outlet guide vane and internal cooling of a blade tip.

1.1 Background

1.1.1 Outlet guide vane

Outlet guide vanes (OGVs) are positioned in the turbine rear frame (TRF) immediately downstream of the low pressure turbine (LPT), providing a structural connection between the aft bearing support and the main engine case, as shown in Fig. 1.1. Aerodynamically, they have a function to straighten the flow of hot exhaust gas which has been swirled during the passage through the turbine. The swirl angle varies depending on the operation point of the engine (taxi, take-off, landing or cruise) and its range can be relatively large. Because a vane is typically optimized for a specific design angle, off-design operation of the OGV leads to flow separation of the hot exhaust gas. The off-design separation usually results in a different heat transfer load which may influence the thermal and life predictions. Therefore, it is imperative for designers to know the local heat transfer coefficients on the vane and the endwall, both for the on- and off-design conditions.
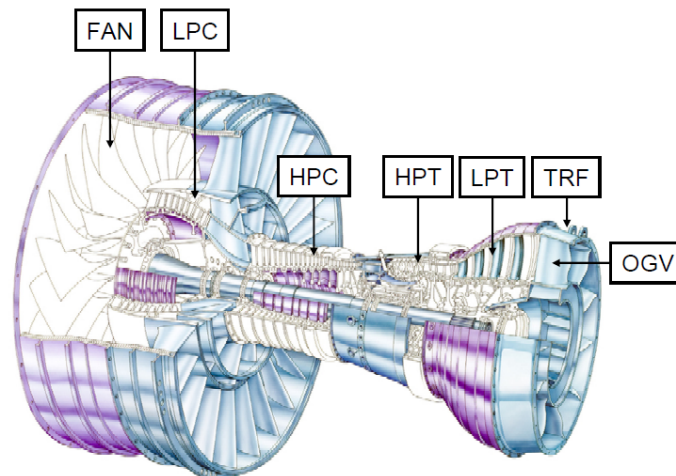
Fig. 1.1 Picture of an ordinary two-spool engine

(Courtesy of GKN Aerospace Engine Systems).

1.1.2 Cooling of a blade

Modern gas turbine engines operate at a high turbine inlet temperature (1200-1500 °C) in order to improve the power and thermal efficiency. Such a temperature is far above the melting temperature of metals and poses a serious problem for engineers to cool the blades. Thus it is imperative to cool turbine blades for a safe and long-lasting operation. Various internal and external cooling techniques have been employed to decrease the blade temperature. Figure 1.2 shows the modern cooling concepts of a gas turbine blade. The leading edge is cooled by jet impingement, the trailing edge is cooled by pin-fins, and the middle portion is cooled by rib-roughened serpentine passages [1].
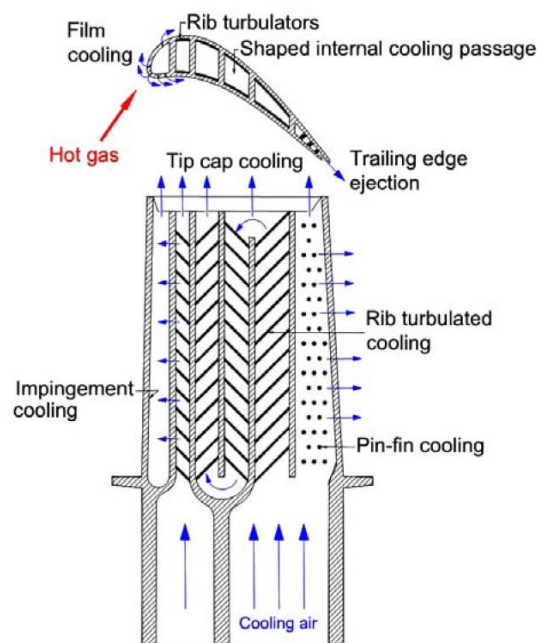
Fig. 1.2 Modern cooling concepts of a gas turbine blade [1].

Cooling of the blade should include the cooling of all regions exposed to high-temperature gas and thermal load. Among such regions, the blade tip area is of particular interest [2-5]. Gas turbine blades usually have a clearance gap between the blade tip and the stationary shroud (or casing) for the sake of blade rotation and the thermal expansion. Due to the pressure difference between the pressure and suction side, the hot gas leaking through the gap will cause a large thermal load on the blade tip and lead to high local temperature. It is therefore essential to cool the turbine blade tip region.

1.2 Literature survey

1.2.1 Heat transfer of outlet guide vanes

In principle, an OGV can be considered comparable to a turbine vane or blade due to the similarity of their shapes and fluid flow around them [6]. The basic mechanisms that affect gas-to-airfoil heat transfer include boundary layer transition behavior, flow separation and reattachment, which are sketched in Fig. 1.3 [7]. At the leading edge there is a very thin laminar boundary layer. On the pressure side, this boundary layer is tripped and there is a transition to a very thin turbulent boundary layer. The favorable pressure gradient accelerates the flow around the leading edge. In some cases the flow separates, a separation bubble is formed and, when the flow reattaches, the boundary layer becomes turbulent. The boundary layer grows under the influence of an adverse pressure gradient and thereafter the flow separates. In the wake, downstream of the trailing edge, the low-speed flow from the separation region on the suction side forms a mixed shear layer with the flow from the very thin boundary layer on the pressure side.
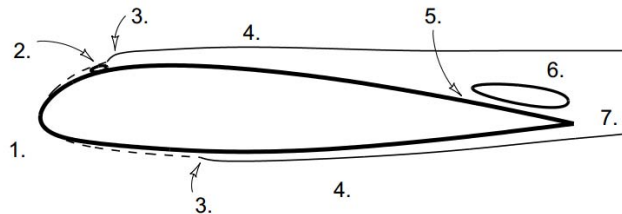

 Fig. 1.3 Schematic sketch of the flow regimes around an airfoil: 1. Laminar boundary layer, 2. Laminar separation bubble, 3. Transition region, 4. Turbulent boundary layer, 5. Separation point, 6. Separation region, 7. Wake region [7].

Extensive investigations have been carried out on the heat transfer of turbine vanes and blades. Nealy et al. [8] were the first to present a comprehensive study of aerodynamic and heat transfer distributions on turbine vanes. The heat transfer characteristics on the airfoil surface were very much dependent on the vane geometry, and the heat transfer increased significantly with increasing Reynolds number. Ames et al. [9, 10] demonstrated the effect of turbulence levels in increasing heat transfer and causing earlier boundary layer transition. Their results also indicated a strong influence of the turbulent length scale on the vane heat transfer. Arts et al. [11] performed detailed aerodynamic and convective heat transfer measurements on a high pressure turbine nozzle guide vane, to study the effect of free stream Mach and Reynolds numbers as well as turbulence intensity. Stripf et al. [12] studied the surface roughness effects on heat transfer of the vane, and the results showed that even the smallest roughness causes the laminar-turbulent transition to move considerably upstream and increases the heat transfer on the vane. Liu and Rodi [13] measured the unsteady surface pressure and heat transfer on a blade exposed to unsteady oncoming wakes. They found that the boundary layer on the suction side became transitional under the wake disturbance. With increasing wake-passing frequency, the start of the transition moved forward, resulting in a significant increase in heat transfer along the whole blade surface including the portions where the boundary layers were nominally laminar. Later, Wissink and Rodi [14] performed Direct Numerical Simulation (DNS) in accordance with these experiments, and found that the heat transfer enhancement

was mainly due to the exchange of hot fluid from the surface of the blade and cold fluid from the free stream by the longitudinal streamwise vortical structures which were triggered by the impinging wakes. Rhee et al. [15] studied the effects of the axial spacing between the vane and the blade on the heat transfer characteristics. Different heat transfer patterns were observed on the blade surface, especially near the blade tip due to the variation in tip leakage flow. However, Blair et al. [16, 17] pointed out that the effects on heat transfer produced by relatively large changes in vane/blade spacing or by changing the relative circumferential positions of the vane/blade were very small. They also conducted turbine heat transfer experiments in a rotating turbine model for various combinations of Reynolds number and inlet turbulence level and for a very wide range of rotor incidence angle. For extremely large negative incidence angles, the flow was completely separated from the rotor pressure surface. In addition, it was demonstrated that on the pressure surfaces of the first-stage vane, combinations of high Reynolds number and high turbulence can produce heat transfer rates well in excess of two-dimensional turbulent flow. It is possible that for certain critical combinations of concave surface curvature, Reynolds number, flow acceleration, and free-stream turbulence level, important Görtler vortex systems are produced in the boundary layer. Ames et al. [18] investigated the influence of incidence angles ranging from -10 degrees to +10 degrees on the performance of the turbine guide vane. Heat transfer along the pressure surface indicated that the location and mode of transition varied with the changing incidence angles. Particularly, Simon [19] and Gaugler [20] considered the laminar to turbulent boundary layer transition phenomenon on turbine vanes/blades, and evaluated the effects of free-stream turbulence, convex and concave curvature, favorable and adverse pressure gradient, roughness, and wake passing by reviewing and analyzing the data based on experiments, DNS and turbulence modeling. Combined with flow visualization experiments, pressure and heat transfer measurements by Meschwitz [21], it was indicated that the flow separated and reattached near the leading edge on the pressure surface for low free stream turbulence. Other investigations with similarly-shaped turbine blades [22, 23] have observed comparable flow behavior in this region.

Despite the resemblance with turbine vane or blade, the OGV has a larger working range to provide an axial outflow for all operating conditions of the turbine, with high turbulence and unsteadiness of the incoming flow. Therefore it is necessary to study OGVs under typical circumstances. Very little work has been undertaken in this field. Koch et al. [6] focused on the numerical and experimental investigation of an optimized OGV at low turbulence intensity with various incidence angles from +10.2 degrees to +38.2 degrees. They presented results of velocity, profile pressure measurements, surface oil flow visualization and transition measurements with a flatted pitot probe. Over a large part of the working range, the position of transition onset across the suction side of the OGV shifted linearly towards the leading edge with increasing incidence angle. The size of the transition region was nearly constant. The position of the transition matched very reasonable with separation bubbles visible in the pressure distributions of the suction side, indicating that the transition is induced by the separation bubbles. The oil flow visualization showed that at the negative limiting incidence angle on the pressure side, there is a separation bubble directly at the leading edge. At two other larger incidence angles +24.2 degrees and +38.2 degrees, there is no separation on the pressure surface and the flow is completely laminar. Hjärne [24] carried out experiments on the aerodynamics around an OGV, both with and without an engine mounted bump. Properties like load

distributions, losses, outlet flow angles and the evolution of the secondary flow field were measured and analyzed for a better understanding of the OGV flows. Chernoray et al. [25] and Lalit et al. [26] experimentally studied the influence of surface non-conformances at different locations on the OGV flow field.

Because in modern gas turbines the endwall region (hub and the shroud) becomes more and more thermally loaded, increasing focus lies on the endwall itself, where secondary flows dominate the heat transfer behavior. The complex vortex pattern of these secondary flows has been investigated by Langston et al. [27]. Figure 1.4 shows the rolling-up of horseshoe vortices as the inlet boundary layer approaches the vanes. Due to the steep pressure gradient, the passage vortices are deflected towards the suction side of a vane.
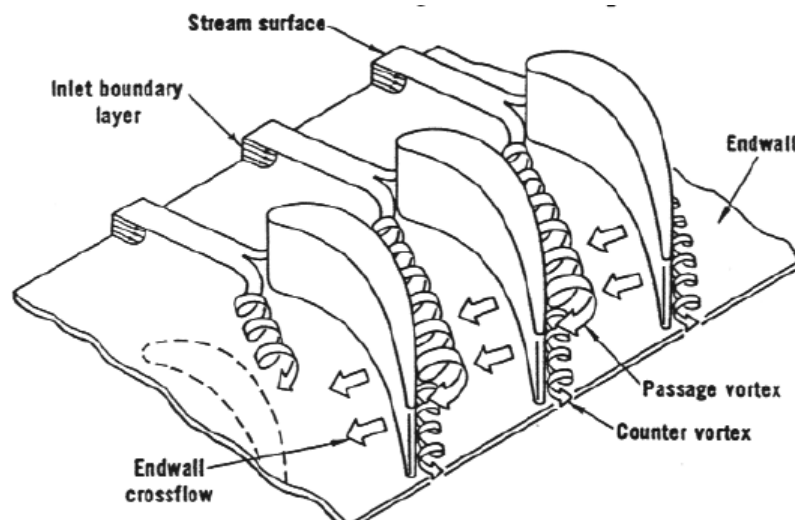

Fig. 1.4   The horseshoe vortices rolling up from the inlet boundary layer, depicted by Langston et al. [27].

Detailed external heat transfer measurements on a smooth turbine blade and endwall by Graziani et al. [28] show strong secondary flow effects on the airfoil and endwall heat transfer. The leg of the horseshoe vortex on the pressure side of the airfoil has been shown to have high aerodynamic losses associated with it [29-31]. The leading-edge region of turbulent juncture flows is of particular interest in turbomachinery applications because the presence of the horseshoe vortex system has been found to increase the local endwall heat transfer rates by as much as 300% above flat plate levels [32-35]. High heat transfer rates in the leading edge regions of high-pressure turbines are known to cause thermal-mechanical fatigue, spalling of thermal barrier coatings, and airfoil endwall/platform burning. Similar results have been obtained by Harvey and Jones [36] and Nicklas [37]. They confirmed the presented heat transfer distribution with an area of high heat transfer in the leading edge region due to the horseshoe vortex, an increase in heat transfer in the channel flow due to the acceleration of the flow, and increased heat transfer in the trailing edge region. Wang et al. [38, 39] investigated the endwall heat transfer of an OGV for the on- and off-design conditions. It was found that remarkable flow separation was noticed for the off-design conditions, indicating that the incidence angle has a significant effect on the endwall heat transfer.

1.2.2 Internal cooling of a blade tip

An effective way to cool the blade and its tip is to design serpentine channels with a 180º turn/bend inside the blade, as shown in Fig. 1.5. The coolant flow coming from the first pass turns 180º and travels from the tip to the second pass. Flow patterns induced by the sharp turn, are impingement, separation, reattachment and secondary flow, which cause a substantial increase in heat transfer, thermal gradients, and pressure loss in the turn region of the internal passages. A better understanding of these processes is beneficial in the improvement of designs. Therefore internal cooling of gas turbine blades with a U-bend channel has been extensively studied.
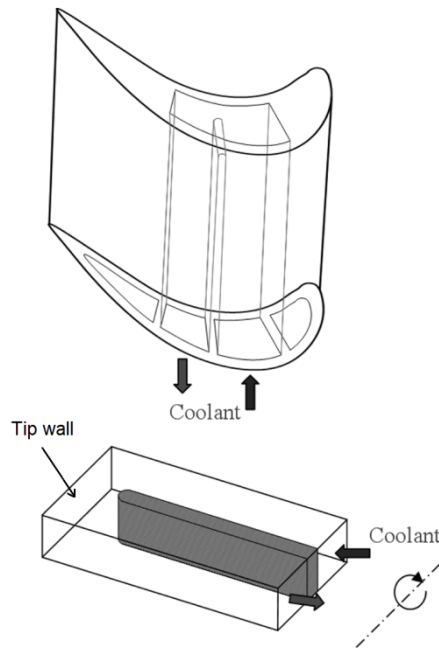

Fig. 1.5 A typical serpentine cooling passage inside a blade.

Metzger el al. [40-43] first investigated the effects of the inlet to outlet channel width ratio, turn clearance and rib arrangements on the overall pressure drop and heat transfer of the two-pass channel. Wang et al. [44] presented numerical results for secondary flow patterns and heat transfer distribution in a two-pass square duct with 180º sharp straight-corner turn, rounded-corner turn, and circular turn. At the turn region, the straight-corner case has the strongest turn-induced heat transfer enhancement, while the circular turn has the weakest. Liou et al. [45, 46] found that the divider wall thickness had profound effects on flow field and heat transfer in a two-pass channel. In addition, the results showed that the direction and strength of the secondary flow with respect to the wall are the most important fluid dynamic factors affecting the heat transfer distributions in the two-pass smooth channel, followed by the convective mean velocity and turbulent kinetic energy. Han et al. [47, 48] performed detailed heat transfer and flow measurements in a two-pass square channel with a smooth wall and a 90º ribbed wall. They concluded that flow impingement is the primary factor in heat transfer enhancement in the bend region. Hirota et al. [49, 50] demonstrated that the turn clearance has a significant effect on the fluid flow and heat transfer in smooth two-pass channels. Lower turn clearance enhanced heat transfer but also produced high pressure drop. Recently Chang and Cai [51] found that the introduction of bleed in the bend region increases the heat transfer enhancement

and reduces the pressure drop. Jenkins et al. [52] and Siddique et al. [53, 54] investigated heat transfer and pressure drop in two-pass channels with varying aspect ratio at different divider wall-to-tip wall distances with and without the presence of ribs. An optimum tip wall position is suggested, forming a compromise between heat transfer improvement and increased pressure losses. Schüler et al. [55] showed that by application of proper turning vanes in the bend region, the pressure loss can be significantly reduced while keeping heat transfer levels reasonably high. Saha et al. [56] found that the bend geometry can have a significant effect on the overall performance of a two-pass channel by comparing six bend geometries. Verstraete et al. [57, 58] addressed the design of a U-bend for serpentine internal cooling channels optimized for minimal pressure losses with numerical methods and experimental validation.

A fairly large literature base exists concerning the augmentation of heat transfer in ribbed straight channels. The ribs break the viscous sublayer and create local wall turbulence due to flow separation and reattachment between ribs, thus enhancing the cooling effect. Continuous and transverse ribs were the most commonly used to investigate the effects of rib height, rib pitch, channel aspect ratio and Reynolds number on the heat transfer and pressure drop [59, 60]. Further studies show that angled and V-shaped ribs provide a better heat transfer performance than transverse ribs due to the secondary flow induced by the ribs [61-63]. Two-pass configurations with ribs in the inlet and/or outlet channel have also been investigated. Chandra et al. [64] and Mochizuki et al. [65] studied the combined effects of a sharp turn and rib configurations on local heat transfer in the smooth and rib roughened ducts with a 180º turn. Ribs were attached on two opposite walls with an angle of 90º or 60º to the flow. Ekkad et al. [66] presented detailed heat transfer distributions for a two-pass square channel with different rib arrangements and with or without bleed hole extraction.

To further enhance the heat transfer in the turn region of the U-bend channel (blade tip region), many efforts have been made. Bunker [67] presented a method to substantially increase the convective heat transfer on the internal cooled tip cap of a turbine blade, where arrays of discretely shaped pins were fabricated and placed. Five tip-cap surfaces were tested and effective heat transfer coefficients based on the original smooth surface area were increased by up to a factor of 2.5. This augmentation method resulted in negligible increase in tip turn pressure drop compared to that of a smooth surface. Xie and Sundén [68, 69] performed several numerical studies of heat transfer enhancement of a blade tip wall with circular pins and dimples. It was suggested that the use of dimples was suitable for augmenting heat transfer and to achieve an optimal balance between thermal and mechanical design requirements. Salameh and Sundén [70, 71] measured the heat transfer in the turn region of a U-bend. They found that the number and position of the ribs had a large impact on the heat transfer and pressure drop. Wang et al. [72, 73] applied 90º ribs with different pitch ratios on the U-bend surface and it was found that the highest heat transfer enhancement factor is obtained at a rib pitch ratio of 12. However, studies on the effects of different rib arrangements in the turn region of the U-bend channel on flow pattern, heat transfer enhancement, thermal gradients, and pressure loss are very few.

1.3 Objectives

The objectives of the work regarding heat transfer of the OGV are:

1. Detailed measurements of the heat transfer coefficient distributions on the vane and endwall, at both on- and off-design conditions.
2. Influence of the incidence angle and Reynolds number on the heat transfer characteristics.
3. Providing experimental results to validate CFD methods for optimizing OGV design.

The study of the internal cooling of blade tip is aimed for:

1. Detailed measurements of the heat transfer coefficients and pressure drop distributions in the turn region of the two-pass channel with and without ribs.
2. Analysis of the combined effects of the sharp turn and ribs on the heat transfer.
3. Evaluation of the thermal performance and heat transfer non-uniformity of different rib configurations.

1.4 Outline of thesis

The introduction of this study is presented in Chapter 1, which includes the background, literature survey and objectives. In chapter 2, the experimental setup and measurement techniques are described. Data reduction and analysis of uncertainties are also described in this chapter. The results are shown and discussed in Chapter 3. Chapter 4 draws the conclusion based on the study, followed by the ideas for the future work.

2 Experimental setup and measurement techniques

2.1 Liquid crystal thermography (LCT)

2.1.1 Introduction to LCT

Liquid crystal thermography (LCT) has been widely used for the visualization and determination of surface temperature distributions leading to convective heat transfer coefficients. Their advantage is that they may cover the complete surface, allowing global temperature distributions to be found.

The sensing ability arises from the molecular structure within the thermochromic liquid crystal materials (TLCs), which possess a special optically active state and reflect incident light selectively over a specific range of wavelengths (color). As selective reflection of the liquid crystal is a function of temperature, the liquid crystal color display can be used as a temperature indicator over a large area. These structures occur when the material is in the temperature range which corresponds to its transition between the solid and liquid states. This transitional temperature range may be broad (20 ^{o}C) or narrow (1 ^{o}C) and the material may flow as a fluid but have anisotropic rheological properties. Many texts on the molecular nature of the materials are available [74]. An account of the relationship between structure and optical activity pertinent to the sensing of temperature is given by Jones [75].

Over the development of LCT, several methods have been employed to interpret color of liquid crystals. Currently, the hue-temperature method is most commonly used due to its high resolution in heat transfer research field. The red, green, and blue (RGB) components of images captured by a CCD are converted into the hue, saturation and intensity (HSI) by computer processing. Among these parameters, the hue value is directly related to the temperature, changing monotonically from 0 to 255 when the temperature of the liquid crystal is increased through its active range.

In general, the liquid crystal technique is non-intrusive, inexpensive and capable of high spatial resolution and accuracy in temperature measurement. However, liquid crystals can only be used at relatively low temperature, i.e., usually below 220 $^{\circ}$C. in addition, a few factors except temperature may affect the liquid crystal color, such as viewing angle, lighting system, camera system, test section properties, etc. When LCT is applied to curved surfaces, e.g., the OGV surfaces in this study, effect of viewing angle/optical access should be considered. Proper calibrations for different viewing angles are therefore essential, to get the relationship between the temperature and hue value.

2.1.2 Calibration of LCT

In the present study, LCT package R35C5W from Hallcrest is used. As heat transfer surfaces are geometrically complex in most of the propulsion applications, the

viewing angle effect during heat transfer measurements on a curved surface needs to be quantified by calibration. Before the execution of the experiment, LCT was calibrated with four different viewing angles (90º, 60º, 45º, and 30º), to obtain the relationship between temperature and hue.

The calibration was performed in a wooden black box in which an aluminum plate was placed. The liquid crystal sheet was applied on the surface of an aluminum plate towards which a CCD camera was directed with a specific angle and two lamps were mounted vertically. On the other side of the plate, six thermocouples were fitted to measure the temperature. The accuracy of the thermocouples is 0.03 °C. The air is heated by a heater which is connected with a fan. The air temperature can be adjusted by controlling the power of the heater. It was found that the non-uniformity of temperature across the aluminum plate was less than 0.1 °C. At a thermal equilibrium state, the LCT image was captured by a CCD camera and the temperature was recorded by a data logger. Thus a calibration curve of one viewing angle could be established. After that, the viewing angle of the CCD camera is changed and the above procedures are repeated. More details of the calibration apparatus and process can be found in Gao [76].

Figure 2.1 shows the calibrated hue-temperature profiles. The green color range is used to measure the wall temperature. It is found that the profiles for viewing angles from 30º to 60º are nearly coincident in the sub-range of hue between 60 and 100, but different from that for a viewing angle 90º. Based on these results, for plate surfaces in the U-bend channel and on the endwall of the OGV, the profile for viewing angle 90º is used to get the temperature. For the curved surfaces on the pressure and suction sides of the OGV, profiles for viewing angles from 30º to 60º are applied to obtain the temperature. The accuracy of this temperature measurement is approximately ±0.2 ºC.
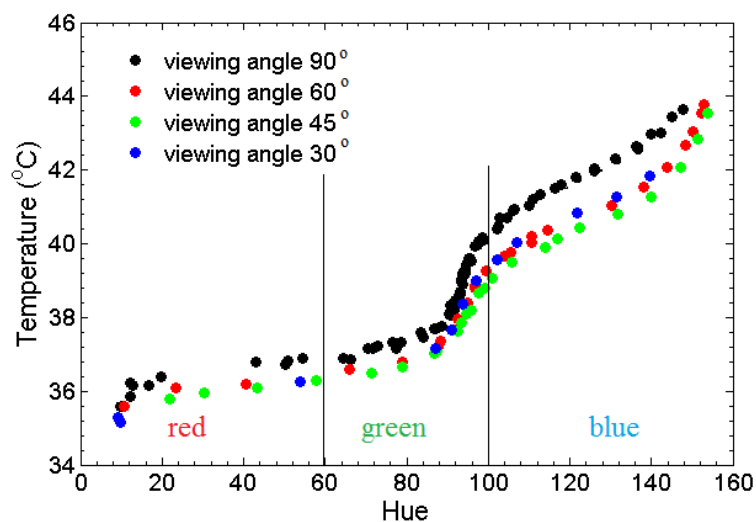
Fig. 2.1   Calibration curves of the LCT.

2.2 Linear cascade

Experiments of the outlet guide vane were performed in a linear cascade facility located at Chalmers University of Technology. The facility is a low-speed blow-down open-circuit linear cascade consisting of a wide angle diffuser (expansion ratio is 4), a settling chamber, a two-dimensional contraction chamber (contraction ratio is 5), an inlet section and a test section with boundary-layer suction, see Fig. 2.2. The flow is driven by a 30 kW centrifugal fan.
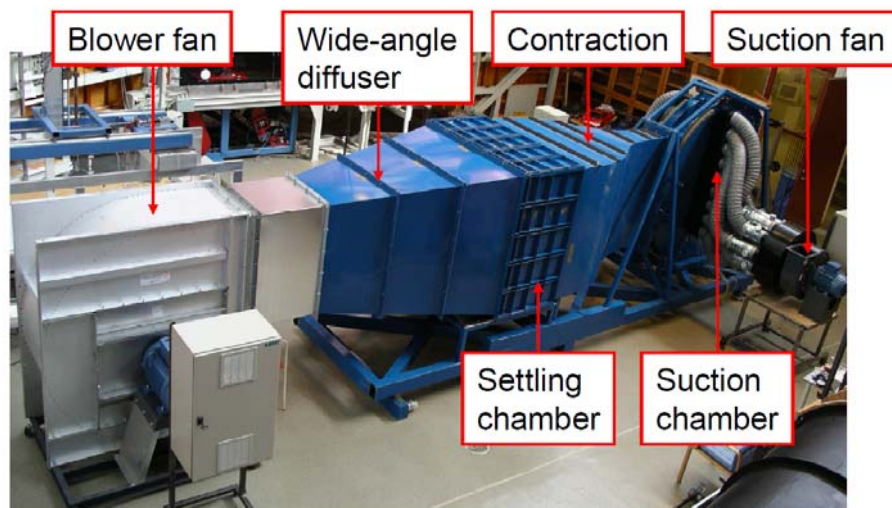

Fig. 2.2   The linear cascade facility.

The test section is designed out of two pairs of parallel discs where the inner discs constitute the upper and lower endwalls of the OGVs, as shown in Fig. 2.3. The inlet flow velocity in the wind-tunnel is monitored by a Pitot-Prandtl tube connected to a digital micro-manometer, which has sensors for temperature and absolute pressure readings. The incoming flow turbulence was adjusted by a turbulence grid which consists of 5 mm bars with a mesh size of 25 mm and was placed 700 mm upstream of the cascade parallel to the leading edge plane. The inlet boundary layer on the sidewall was carefully controlled. The natural boundary layer was removed by the upstream suction system and the new turbulent boundary layer was generated by a trip-wire. The cross section of the working area of the facility is 240 mm by 1200 mm. The cascade has 6 OGVs and the pitch between two adjacent vanes is 240 mm. The vane axial chord is 243 mm and the span is 240 mm. The three middle vanes are instrumented with pressure taps at the mid-span. The flow periodicity in the cascade is controlled by the tail-boards attached to the topmost and bottommost vanes. Before the heat transfer measurements, the flow periodicity was checked by measuring the static pressure distributions at the mid-span of the three central vanes. Surface static pressure distributions are measured by a 16-channel PSI 9116 digital pressure scanner (Pressure System Inc.) which has a measuring range of ±2500 Pa. More details concerning the design and validation of the linear cascade can be found in [24]. In the current study the Reynolds numbers are 300,000 and 450,000 and the corresponding incoming velocities are around 20 m/s and 30 m/s, respectively. The level of the flow turbulence intensity was 3.5% and the turbulence length scale is 1.2 mm. The flow incidence angles are adjusted to be +40 degrees, +25 degrees, and -25 degrees.
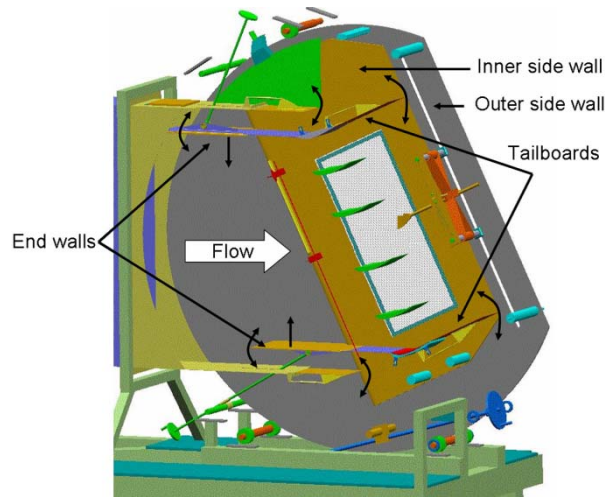
Fig. 2.3   The test section of the cascade.

2.2.1 Measurements on the OGV

The OGV consists of a two-dimensional profile section which is extended in the span direction. Figure 2.4 shows the cross section of an OGV profile. The geometry is representative for a typical structural OGV with a blunt leading edge. Cascade vanes are manufactured using stereo-lithography technique, which has a typical accuracy of ±0.1% of the model size. The surfaces of the vanes were polished and painted. The thermal conductivity of the vane material is close to 0.2 W/mK.
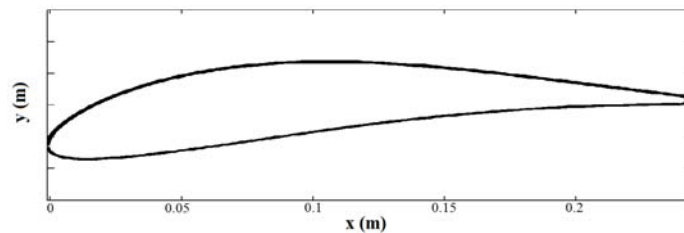

Fig. 2.4   The cross-section profile of an outlet guide vane.

Endwalls in the cascade are made of acrylic glass, which provided an optical access for the CCD camera. Heat transfer measurements were performed at the middle vane in Fig. 2.3. Both the pressure and suction sides were covered by the heating foil and were referred to as the heat transfer target wall. The size of the heater is 500 mm by 240 mm. The heater was made of an etched constantan foil. The constantan was selected due to its low temperature coefficient of resistance. The width of the conductive pathway is 7.32 mm and the gap between two neighboring pathways is 0.20 mm. Due to the gaps between the pathways, the heat flux across the span of the heater is not perfectly uniform (the non-uniformity is estimated to be less than 3%). The surface temperature was measured by an LCT sheet that was 500 mm by 160 mm and placed in the middle of the vane. The LCT sheet, R35C5W was manufactured by LCR Hallcrest Ltd. Before the experiments, the LCT sheet was calibrated to obtain the relationship between the temperature and the hue for different viewing angles. Two lamps (MASTER TL-D Super 80) were used as the illuminating light. The LCT images were captured by a GigE Vision CCD camera which allows 1600 by 1200 pixel resolution. During the experiment, the CCD camera, illumination lighting, and

the test section were covered by a dark enclosure to prevent interference from the surrounding light noise. Figure 2.5 shows the LCT images in the test section where a steady state has been reached.
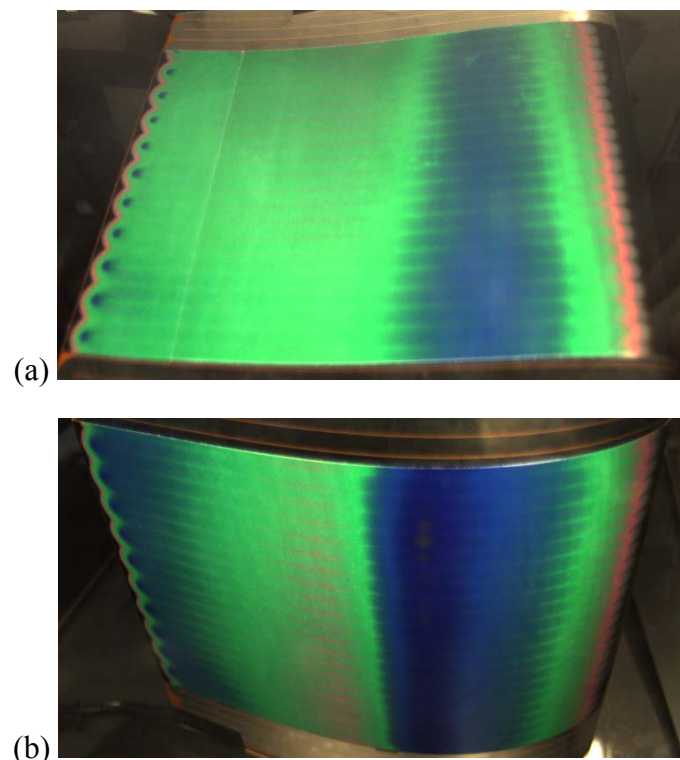

(a)

(b)

Fig. 2.5   The LCT images of OGV in the test: (a) pressure surface; (b) suction surface. The flow is from right to left.

After each heat transfer test, a grid paper was adhered smoothly to the LCT sheet on the vane. Another picture was taken by the camera at the same position as during the test. The grids on the paper were 10 mm squares. With proper image processing and calculation, the heat transfer data at the mid-span of the vane could be obtained conveniently.

2.2.2 Measurements on the endwall

Endwalls in the cascade are made of Plexiglas, which provided optical access for the CCD camera. Heat transfer measurements were performed on the endwall of the middle cascade passage, extending from the middle vane to the adjacent two vanes, as shown in Fig. 2.6. The thickness of the endwall is 20 mm and the thermal conductivity of the material is 0.2 W/mK. Part of the endwall is covered by a heating foil and is referred to as the heat transfer target wall. The size of the heater is 500 by 320 mm. The heater is made of an etched constantan foil. The width of the conductive pathway is 4.87 mm and the gap between two neighboring pathways is 0.27 mm. Due to the gaps between the pathways, the heat flux across the span of the heater is not perfectly uniform (the non-uniformity is estimated to be less than 5%). The surface temperature is measured by an LCT sheet which was the same size as the heater. A CCD camera and illuminating light are used in the same way as those for OGV heat transfer measurements. Figure 2.6 shows an LCT image (taken by a conventional camera) in the test section where a steady state has been reached.
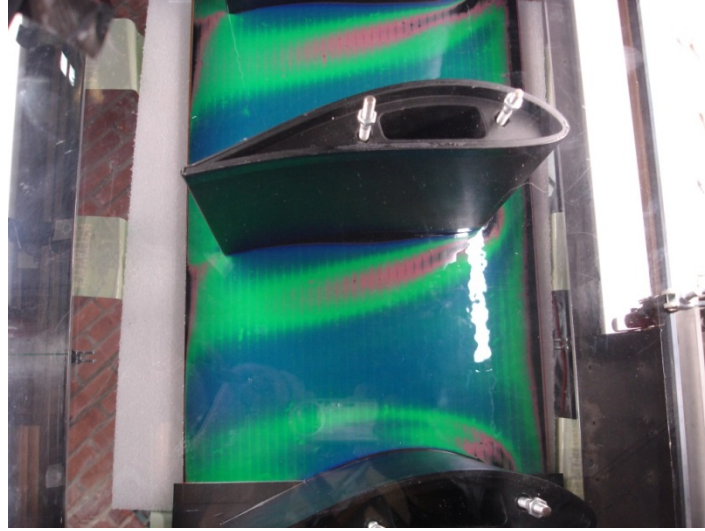
Fig. 2.6 The LCT images of the endwall in the test. The flow is from right to left.

2.2.3 Data reduction and uncertainty analysis

The Reynolds number is defined as:

$$\mathrm{Re} = U_0 L / \nu \tag{1}$$

where U_0 is the axial velocity of the OGVs, L is the vane axial chord length, and ν is the kinematic viscosity of air. The axial velocity U_0 is the product of the free stream velocity U_∞ and $\cos(\alpha)$, where α is the incident angle of the vane. In this study, the Reynolds numbers are 300,000 and 450,000, respectively.

The heat transfer coefficient h, is calculated based on the Newton's law of cooling, i.e.,

$$h = (q_w - q_{loss}) / (T_w - T_{in}) \tag{2}$$

where q_w is the total heat flux, q_{loss} is the heat flux loss, and T_w and T_{in} are the wall temperature and the inlet air temperature, respectively. When calculating the heat flux q_{loss}, the radiative and conductive heat losses are estimated. The LCT is coated with a Mylar film with an emissivity 0.89. It is found that the radiative heat loss is less than 5%. The heat conduction loss is quite low (less than 1%) and is negligible.

The heat transfer coefficient h is obtained in the following manner. After steady state has been achieved, a number of LCT images are generated with a certain viewing angle of the CCD camera, each corresponding to a distinct wall heat flux. In measuring the temperature, the green colour is chosen as the reference colour. By proper adjustment of the wall heat flux, the reference colour is moved from one location to another such that the entire area of interest is eventually covered with the reference colour. Thereby the heat transfer coefficient over the entire area can be obtained. More details of the LCT technique for obtaining the heat transfer coefficients can be found in [76, 77].

The heat coefficient is represented in terms of Nusselt number Nu, which is defined as:

$$Nu = hL \, / \, k \tag{3}$$

where k is the thermal conductivity of air. An uncertainty analysis is performed by applying the method proposed by Moffat [78]. The uncertainty in the local heat transfer coefficients is estimated to be within 8% based on the 95% confidence level. This value takes into account the effects of the errors in the heat flux, bulk temperature and wall temperature, processing system errors associated with the LC images, and errors associated with the lack of repeatability caused by random disturbances and unsteadiness.

The static pressure on the vane is represented in terms of the pressure coefficient C_p, which is defined as:

$$C_p = (P_s - P_{s,in}) / P_{dyn,in} \tag{4}$$

where P_s is the static pressure on the vane, $P_{s,in}$ and $P_{dyn,in}$ are the static and dynamic pressure of the inlet flow, respectively. The accuracy of the surface pressure scanner in the measurement range of the current experiment (± 250 Pa) is ± 2 Pa. For the pressure coefficient, the accuracy is ± 0.01 in non-dimensional units.

2.3 U-bend channel

Figure 2.7 shows the schematic of the experimental setup. The test rig is a U-bend channel which consists of three sections, i.e., inlet section (1.5 m long), turn section (240 mm long), and outlet section (1.5 m long). The flow was maintained by a suction fan attached to the channel outlet. A contracted bell mouth was installed at the inlet passage to provide a smooth entrance flow. The area ratio of the inlet contraction is 4:1. The cross-section dimension of both inlet and outlet passes is 50×50 mm. This results in a hydraulic diameter D_h of 50 mm. In the turn region, the outer wall length W_{out} is 240 mm and the inner wall length W_{in} is 140 mm. The spacing H between the outer and the inner wall is 50 mm.
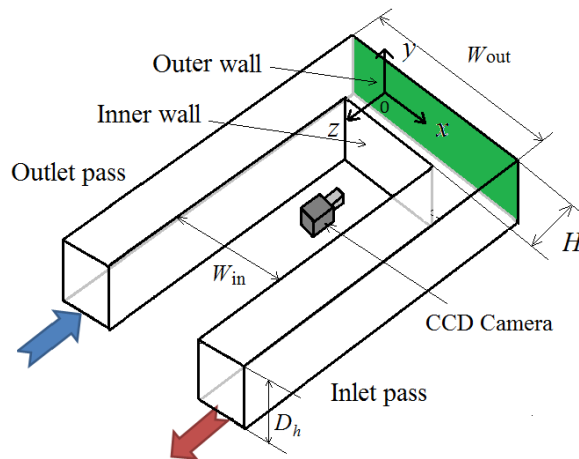
(a) Three dimensional view (lengths not to scale)
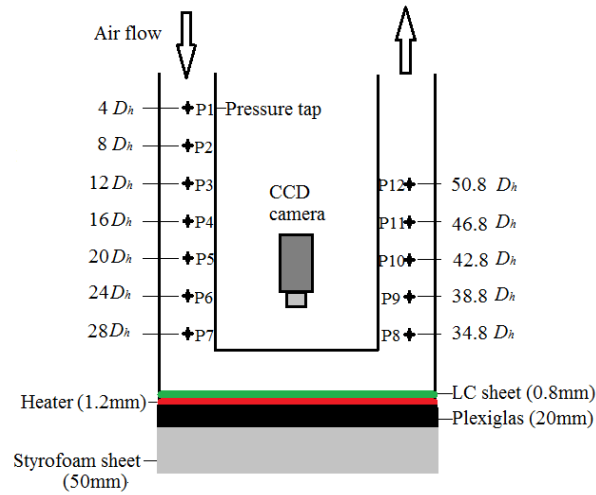
(b) Top view

Fig. 2.7 Schematic illustration of the experimental setup for the U-bend channel.
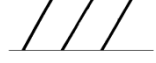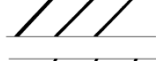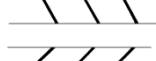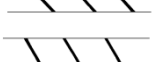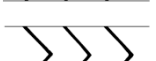
2.3.1 Measurement on the outer wall

The outer wall was covered with a heater and was referred to as the heat transfer plate. The heater was an Inconel foil etched in a serpentine pattern with a 0.1 mm gap between adjacent strips. In order to minimize the heat conduction loss to the environment, a 50 mm-thick Styrofoam sheet was used to cover the back of the outer wall. Above the heater surface, an LC sheet (R35C5W, LCR Hallcrest Ltd) was used to measure the local surface temperature. A CCD camera was placed in the region between the inlet and outlet passages, as shown in Fig. 2.7. The channel was made of Plexiglas to provide optical path for the LC measurements. A steady-state LC technique was used to measure the heat transfer coefficients on the target plate. More details concerning this technique can be found in [76, 77]. In the turn region, the x-axis is along the streamwise direction, the y-axis is the spanwise direction, and the z-axis is normal to the outer wall. During the experiments, because parts of the vision of the CCD camera (especially the two corner regions at the turn) were blocked by the side walls of the channel, the effective heat transfer measurement region was 140 mm ($2.8D_h$) by 50 mm, i.e., the central part of the outer wall. The origin of coordinate O is therefore placed on the outer wall at the location corresponding to the upstream tip of the inner wall, as shown in Fig. 2.7.

The air flow rates were measured by a rotameter with an accuracy of 3% of the full measurement range. The pressure distributions in the channel were measured in separate experiments with unheated flow. The 12 static pressure tap locations along the center line on the top wall are illustrated in Fig. 2.7. The pressure taps were connected by rubber tubes to a micromanometer with an accuracy of 1% of the full measurement range.

Heat transfer in the smooth turn region of the two-pass channel and pressure drop distributions were measured. Then periodic square ribs made of Plexiglas were fitted onto the outer wall in the turn region. Seven rib configurations were studied: 90° ribs, 45° and 60° angled ribs, 45° and 60° V-shaped ribs with the tip facing upstream and downstream. The rib blockage ratio was $e/D_h = 0.06$ (e stands for the rib height) and

the rib pitch to the rib height ratio, *P/e*, was fixed at 12. Owing to their low thermal conductivity, the ribs were considered to be virtually adiabatic and their principal function was to disturb the flow and enhance the heat transfer. One smooth and seven different ribbed turn regions were tested for two Reynolds numbers of 20,000 and 26,000, respectively. The eight test cases are presented in Table 2.1.

Table 2.1 Test cases for the present investigation.

Case No.	Outer wall conditions	Configurations
1	smooth	
2	90º ribbed	
3	60º ribbed	
4	45º ribbed	
5	60º V-shaped-upstream ribbed	
6	45º V-shaped-upstream ribbed	
7	60º V-shaped-downstream ribbed	
8	45º V-shaped-downstream ribbed	

2.3.2 Data reduction and uncertainty analysis

The Reynolds number is defined as:

$$\mathrm{Re} = U_0 D_h / v \tag{5}$$

where U_0 is the air bulk velocity measured by the rotameter and v is the kinematic viscosity of air. The properties of air were calculated at 300 K. In this study, the Reynolds numbers tested were 20,000 and 26,000, respectively.

The heat transfer coefficient is calculated as:

$$h = (q_w - q_{loss})/(T_w - T_0) \tag{6}$$

where q_w is the total heat flux generated by the heater, q_{loss} is the conductive and radiative heat losses (about 4% of the total heat flux), T_w is the outer wall surface temperature measured by the LC, T_0 is the air bulk temperature which is the arithmetic mean value of the inlet and outlet temperature. The inlet temperature T_{in} was measured by a PT100 thermometer with an accuracy of 0.03 °C and the outlet temperature T_{out} was calculated based on the heat balance, i.e.,

$$T_{out} = (q_w - q_{loss}) \cdot A / (mc_p) + T_{in} \tag{7}$$

where A is the heating surface area, m is mass flow rate, and c_p is the air specific heat. Due to the large flow rate and limited heated surface area, the largest temperature rise between T_{out} and T_{in} is only 1 °C in the experiments.

The Nusselt number is thus defined as:

$$\mathrm{Nu} = hD_h/k \tag{8}$$

where k is the air thermal conductivity. The Nusselt number can be normalized by Nu_0 which is predicted by using the Dittus-Boelter correlation [79]:

$$Nu_0 = 0.023 \cdot \mathrm{Re}^{0.8} \cdot \mathrm{Pr}^{0.4} \tag{9}$$

where Pr is the Prandtl number. The normalized Nusselt number Nu/Nu_0 is helpful because it represents the level of enhancement over a straight smooth channel by may collapse the general effects of changes in Reynolds number to highlight local changes in flow behavior.

The local pressure drop is non-dimensionalized by normalizing with the mainstream fluid dynamic pressure head as:

$$K = \frac{P_i - P_0}{\rho U_0^2 / 2} \tag{10}$$

where P_0 and P_i are the ambient pressure outside the channel and local pressure in the two-pass channel measured by each pressure tap, respectively.

The overall pressure drop over the turn is presented in terms of the Darcy friction factor, i.e.,

$$f = \frac{(\Delta P/L)D_h}{\rho U_0^2 / 2} \tag{11}$$

where ΔP is the pressure drop across the turn, between P1 and P12. L is the streamwise distance along the centerline of the two-pass channel between the two pressure taps. The pressure penalty can be determined by normalizing the friction factor by the well-known Blasius equation:

$$f_0 = 0.316 \times \mathrm{Re}^{-0.25} \tag{12}$$

The thermal performance factor is determined by dividing the overall averaged normalized Nusselt number by normalized friction factor [80]:

$$\eta = (\overline{Nu}/Nu_0)/(f/f_0)^{1/3} \tag{13}$$

This thermal performance factor helps to quantify the balance of heat transfer increase against pressure drop penalty and is helpful for determining the optimal rib configuration.

The non-uniformity of heat transfer distribution is examined by comparing the calculated standard deviations of the normalized Nusselt number distributions:

$$(Nu/Nu_0)_{Std} = \sqrt{\sum_{i=1}^{N} (Nu_i/Nu_0 - \overline{Nu}/Nu_0)^2 / N} \qquad (14)$$

where Nu_i is the local Nusselt number at each measuring point, and N is the total number of measuring points on the outer wall captured by the CCD camera. The non-uniformity effect (high standard deviations) of the heat transfer distributions causes large temperature gradients and thermal stresses which are detrimental to the life time of the components, and should be considered during design.

The estimation of uncertainty values is based on a confidence level of 95% and the relative analysis method proposed by Moffat [78]. The uncertainty in heat transfer coefficients was estimated to be 10% by taking into account several sources of error: total heat flux (voltage and current readings), inlet air temperature and outer wall temperature, processing system errors associated with the LC images, and errors associated with the lack of repeatability caused by random disturbances and unsteadiness. Using the maximum uncertainty values of 4% for the measured pressure drop and 3% for the air flow rate, the maximum value of the relative uncertainty of the friction factor was calculated to be 8%.

3 Results and discussion

3.1 Outlet guide vane

3.1.1 Pressure distributions on the OGV

Figure 3.1 presents the pressure coefficient distribution at the mid-span of the OGV. The Reynolds number is 300,000 and incidence angle is +25 degrees, corresponding to the on-design condition. The surface distance is normalized by the vane chord length L. From the definition of pressure coefficient C_p in Eqn. (4), the point at $C_p = 1$ reveals the location of the stagnation point on the vane. In Fig. 3.1, the stagnation point occurs in the immediate vicinity of the leading edge on the pressure surface, between $x/L = 0$ and 0.02.
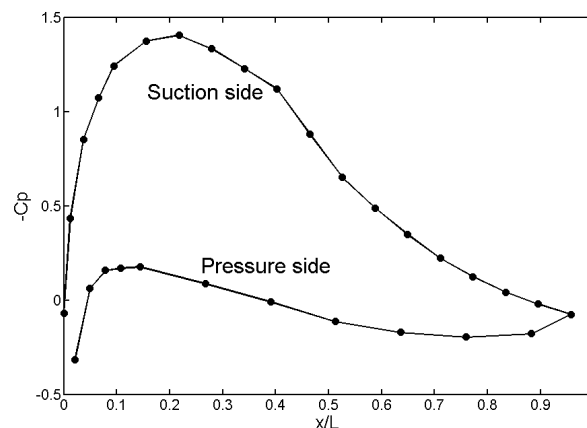

Fig. 3.1   Pressure coefficient at the mid-span of the OGV. Re = 300,000, incidence angle +25 degrees.

The shape of the C_p curve illustrates the behavior of the local velocity of the flow around the vane. On the pressure surface, there is a sharp decrease of C_p from the leading edge to about $x/L = 0.1$, corresponding to a favorable pressure gradient and acceleration of the flow along the surface. After that, the flow decelerates smoothly until $x/L = 0.8$, followed by a slight acceleration just at the trailing edge. On the suction surface, the overall general trend of C_p is quite similar to that on the pressure side. Initially, the local flow accelerates strongly to the "throat" of the cascade passage, which is approximately at $x/L = 0.2$. Then an adverse pressure gradient decelerates the flow in the diffuser region as it approaches the trailing edge. Further inspection of the pressure distribution on the suction side shows that a small 'bump' exists at $x/L = 0.4$, implying that the laminar boundary layer undergoes a transition to a turbulent flow. Our numerical simulations (not shown here) display a transitional separation bubble in this region where the laminar boundary layer separates from the wall. Due to the unsteady vortex shedding in the separated shear layer, the flow becomes fully turbulent before it reattaches on the wall. The heat transfer on the

suction side of the vane is strongly affected by the flow transition, which will be demonstrated later.

3.1.2 Heat transfer distributions on the OGV

Figure 3.2 presents the Nusselt number contours on both the pressure surface and suction surface of the OGV, for on-design condition at Re = 300,000. Note that the region of heat transfer measurement is located in the middle of the OGV, covering 67% of the span width. In order to capture most part of the vane surface, a very small area neighboring the leading edge was lost. Generally the heat transfer pattern is two dimensional, indicating that the horseshoe vortex induced by the endwall boundary separation does not affect the main part of the vane. Also the symmetry shows that the calibrations of the LCT for different viewing angles are valid. For the on-design condition at Re = 450,000, the heat transfer contours on the OGV were quite similar, but they are not given here.
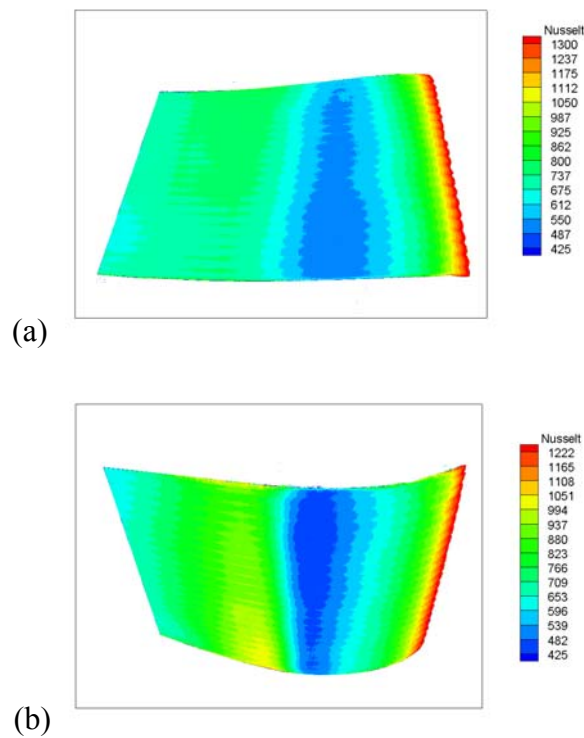

(a)

(b)

Fig. 3.2   Nusselt number contours on the OGV: (a) pressure side; (b) suction side. Flow from right to left. Re = 300,000, incidence angle +25 degrees.
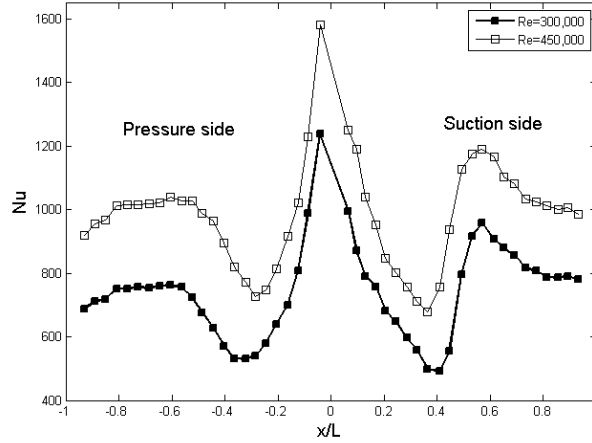
Fig. 3.3 Nusselt number profiles at the mid-span of the OGV. Re = 300,000 and 450,000, incidence angle +25 degrees.

Figure 3.3 gives the Nusselt number profiles at the mid-span of the OGV at Re = 300,000 and 450,000 for the on-design condition. In both cases, as expected, heat transfer is the highest at the stagnation point on the pressure side due to the very thin boundary layer. Incoming flow impinges at this point and is spited into two parts by the vane. Then the heat transfer rate drops appreciably along both the pressure side (negative x/L) and suction side (positive x/L), typical of laminar boundary layer heat transfer behavior. On the pressure side, there is a gradual rise in the Nusselt number beginning at $x/L = -0.32$, indicating the onset of a smooth transition to a turbulent boundary layer. The transition process ends at $x/L = -0.56$. Further downstream, there is a very slight decrease in heat transfer, which can be attributed to the growing thickness of the turbulent boundary layer. On the suction side, the local minimum of Nusselt number at $x/L = 0.41$ indicates that the flow undergoes a transition from laminar boundary layer flow to turbulent flow. The transition position at $x/L = 0.41$ is in good agreement with the results of the pressure measurement shown in Fig. 3.1. It should be pointed out that the transition location on the suction side is a little farther from the stagnation point than its position on pressure side. This difference in the onset location may be caused by the stronger pressure gradient on the suction side. Also the surface curvature on the OGV affects the transition process. At low free-stream turbulence, the experimental work of Wang [81] and Kim and Simon [82] demonstrated that, compared to a flat surface, a convex surface (suction side) will delay the transition onset and a concave surface (pressure side) will shift the transition onset in the upstream direction. This effect of curvature diminishes as the free-steam turbulence increases. In the current study, free-stream turbulence is 3.5%, which is relatively low. Downstream of the onset of flow transition, the Nusselt number reaches a peak at $x/L = 0.57$. Then the heat transfer drops continuously until the trailing edge. Effects of Reynolds number on the heat transfer of the OGV are shown by comparing the Nusselt number profiles for Re = 300,000 and 450,000, respectively. Apparently, the heat transfer coefficients over the entire OGV increase with an increase of Reynolds number. A careful examination indicates that the higher Reynolds number tends to move the transition slightly upstream. Overall, the general trends of the heat transfer distributions are more or less similar.

For certain cases, the incidence angle of the OGV departs greatly from the on-design condition. As a result, it would be of interest to investigate the heat transfer characteristics on the vane for off-design condition. Figure 3.4 shows the Nusselt number contours on the OGV at Re = 300,000. The incidence angle is -25 degrees. On the pressure side the heat transfer is slightly larger at the mid-span and decreases towards the sidewalls. On the suction side the spanwise wave-like modulation has become stronger. These three-dimensional flows may be caused by boundary layer separation on the two endwalls.
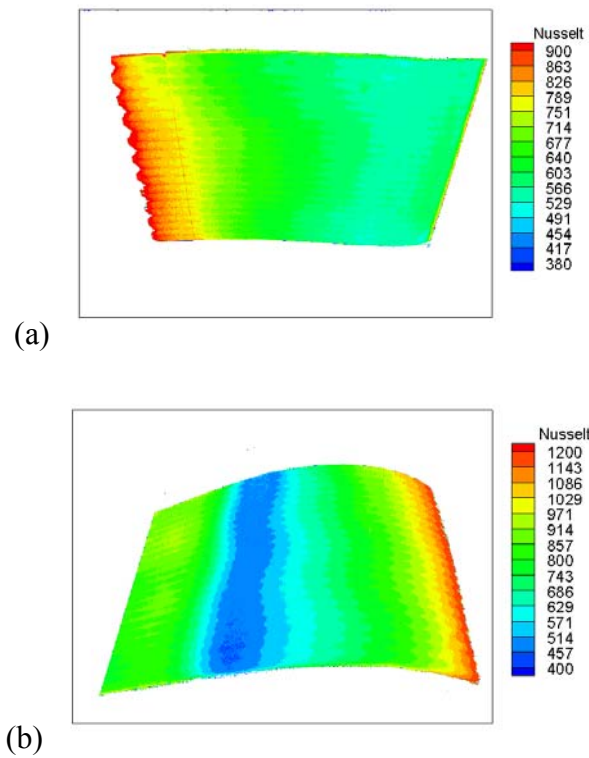

(a)

(b)

Fig. 3.4 Nusselt number contours on the OGV: (a) pressure side; (b) suction side. Flow from right to left. Re = 300,000, incidence angle -25 degrees.
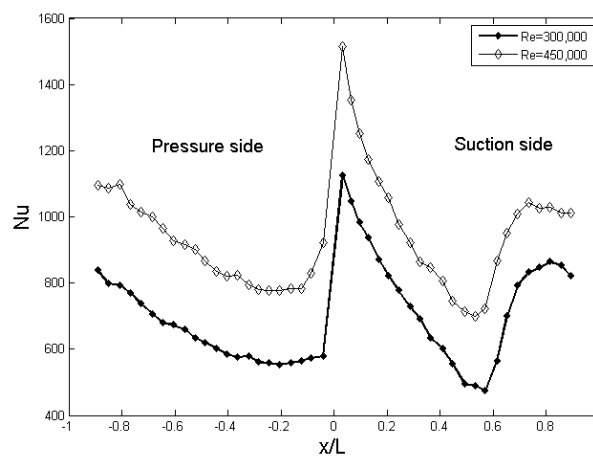

Fig. 3.5 Nusselt number profiles at the mid-span of the OGV. Re = 300,000 and 450,000, incidence angle -25 degrees.

Figure 3.5 presents the heat transfer distributions in terms of Nusselt number at mid-span for off-design condition. Similar to the on-design condition, the Reynolds number increases the magnitude of the Nusselt number but without changing the heat transfer pattern. Due to the change of incidence angle from +25 to -25 degrees, the stagnation point moves from the pressure side to the suction side, leading to the maximum Nusselt number at x/L = 0.03. On the suction side, the laminar boundary layer develops from the stagnation point. Then the heat transfer drops to a local minimum just before the transition onset at x/L = 0.57. Subsequently there is an increase in heat transfer. The small decrease at the trailing edge is caused by growth of turbulent boundary layer thickness. On the pressure side, Nusselt number reduces very sharply within a small distance (from the leading edge to x/L = -0.04). This is quite different from the heat transfer behavior of the laminar boundary layer on the suction side. After this sharp decrease, the Nusselt number increases continuously towards the trailing edge. This is also distinct from that on the suction side. At this extreme negative incidence angle, the heat transfer may be dominated by a large separation region, which starts directly from the leading edge on the pressure side. The separation region occurs because the position of the stagnation point is located on the suction side. The flow cannot follow the high turning at the leading edge. This separation causes a big decrease in the heat transfer rate. Due to the separated shear layer, probably there is an induced low-speed recirculation zone inside the separated region, which has the property of a turbulent flow. All these discussed phenomenona need to be confirmed by flow measurements, which will be conducted in future work.
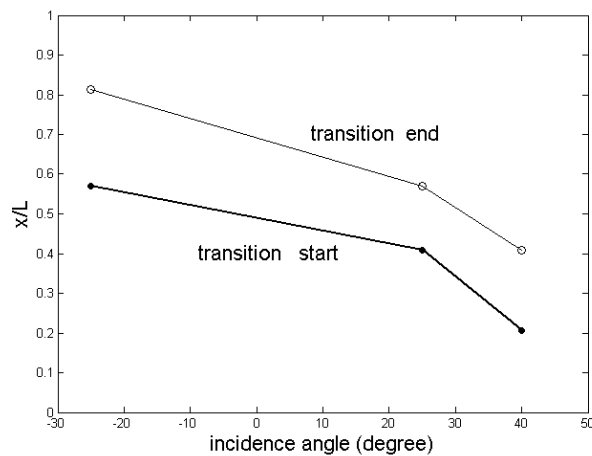

Fig. 3.6   Transition behavior on the suction side of the OGV.

As illustrated above, the transition from laminar to turbulent boundary layer has a significant impact on the heat transfer pattern of the OGV. Effects of free steam turbulence, convex and concave curvature, favorable and adverse pressure gradient, roughness, wake passing, Reynolds number, incidence angle and the stagnation point should be evaluated and considered to improve the understanding of transition in a real engine environment [19]. Here Fig. 3.6 displays the impact of the incidence angle on the onset and size of the transition on the suction side. As the incidence angle decreases from +40 degrees to +25 degrees, the transition onset is shifted downstream. However, the dimension of the transition region is kept constant. With a further decrease of the incidence angle to -25 degrees, the transition moves towards the trailing edge and its length increases.

3.1.3 Heat transfer distributions on the endwall

Figure 3.7 shows the Nusselt number contours on the endwall of an OGV at Re = 300,000. In this figure, the flow is from right to the left. For the on-design condition at the incidence angle +25 degrees, the vane, to a large extent, looks like a "streamlined" object. The flow is split into two parts by the vane and there is no noticeable flow separation observed in this figure. In addition, Fig. 3.7 shows that the heat transfer decreases in the streamwise direction. This can be attributed to the fact that the wall boundary layer grows along the vane chord.

Fig. 3.7 Nusselt number contours on the endwall. Re = 300,000, incidence angle +25 degrees.

Figure 3.8 displays the endwall Nusselt number contours at the incidence angle +40 degrees. In this case, the vane acts more like a bluff body. The boundary layer on the endwall separates at the leading edge of the vane. Heat transfer attains the maximum around the leading edge region, due to the generation of a horse shoe votex. In the pitchwise direction between two adjacent vanes, the heat transfer coefficients decay quickly because the effect of the horse shoe votex on the endwall heat transfer is insignificant.
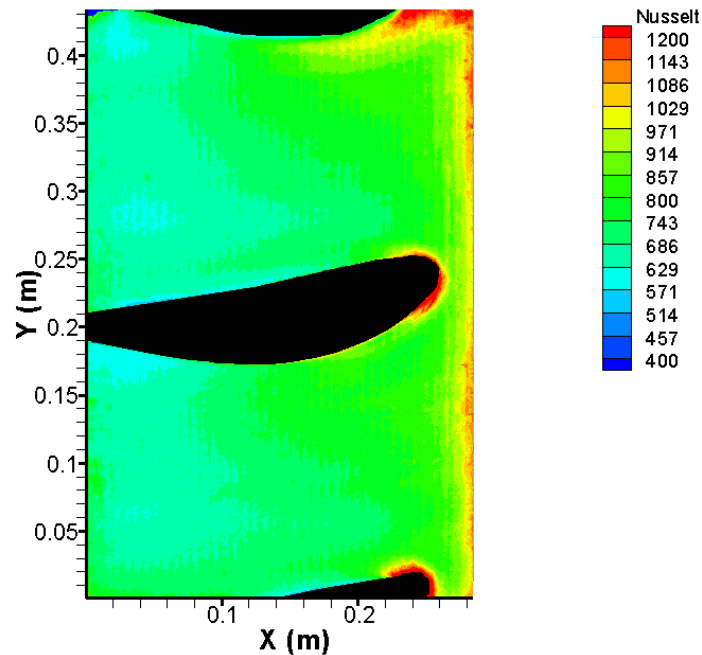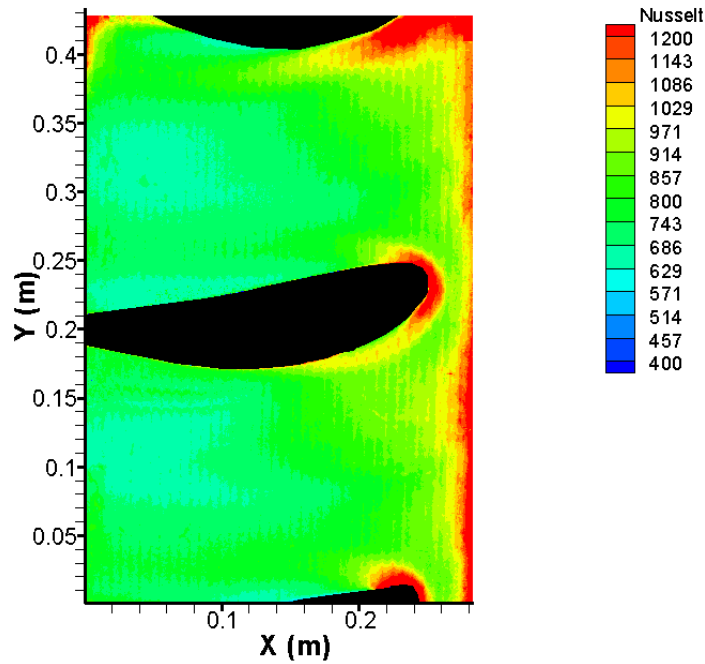
Fig. 3.8 Nusselt number contours on the endwall. Re = 300,000, incidence angle +40 degrees.
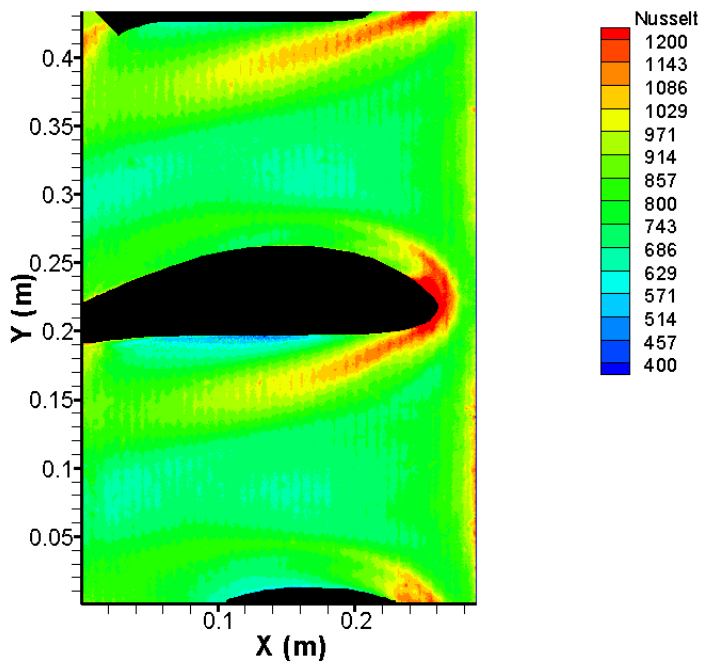
Fig. 3.9 Nusselt number contours on the endwall. Re = 300,000, incidence angle -25 degrees.

For certain cases, the incident flow angle departs greatly from the OGV on-design condition. As a result, it is of interest to know the thermal load and heat transfer coefficients on the endwall. Figure 3.9 shows the endwall Nusselt number contours as the incidence angle is -25 degrees with respect to the vane axial chord. In this case, a

remarkable flow separation phenomenon is observed. On the pressure side, a big bubble is formed between the vane and the separated shear layer. Because the fluid flow in the bubble region is nearly stagnant compared to the mainstream, the local heat transfer coefficients are quite low. At the leading edge of the suction side, the heat transfer attains its maximum due to the impingement effect of the main flow.

3.2 U-bend channel

3.2.1 Pressure drop distributions

Figure 3.10 shows the non-dimensional pressure drop distributions of a U-bend channel with smooth (case 1) and ribbed (cases 2 – 8) turn regions at Re = 20,000. For all the cases at Re = 26,000, the general pressure distributions are quite similar, but they are not given here.
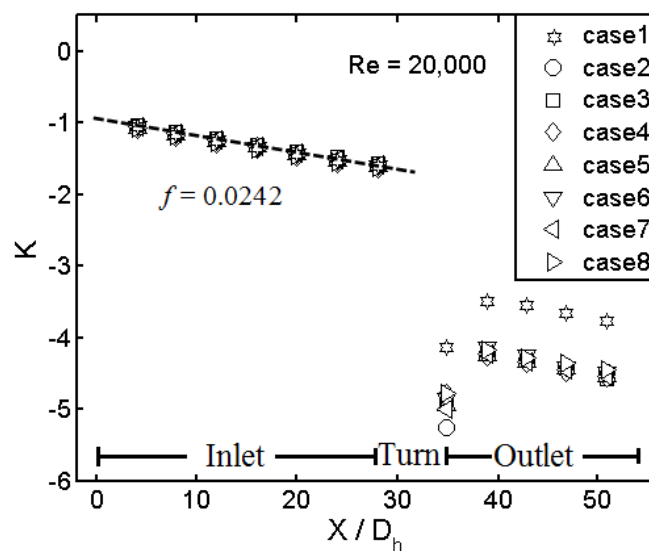
Fig. 3.10 Local pressure drop distributions of a U-bend channel with smooth and ribbed turn regions at Re = 20,000.

It can be seen that in the inlet of the U-bend channel, all the cases show the same local pressure distributions. The constant pressure drops are clearly visible and their linear regressions are used to determine the friction factor $f = 0.0242$, which is very close to the prediction of Blasius equation. This indicates that the flow has reached the developed turbulent state in the inlet and is not affected by the ribs in the turn region. Just after the smooth turn region (case 1), the pressure decreases steeply to a minimum and then recovers quite a bit due to the turn-induced separation bubble. Thereafter, the pressure begins to drop again. This pressure drop distribution is in line with that measured by Metzger et al. [40]. For the ribbed cases 2 to 8, the overall pressure distributions in the outlet are somewhat similar to those of the smooth case. However, it should be noted that the ribs cause a relatively larger pressure drop over the turn region.

3.2.2 Heat transfer on the outer wall

Before considering the effects of different ribs, it is necessary to establish a baseline of the heat transfer distributions in the turn region of the smooth U-bend channel without ribs. Figure 3.11 provides the heat transfer distributions on the smooth outer wall at Re = 20,000. The Nusselt number is normalized by the values for the fully developed turbulent heat transfer in a smooth straight channel using the Dittus-Boelter equation. All lengths are scaled by the hydraulic diameter D_h.
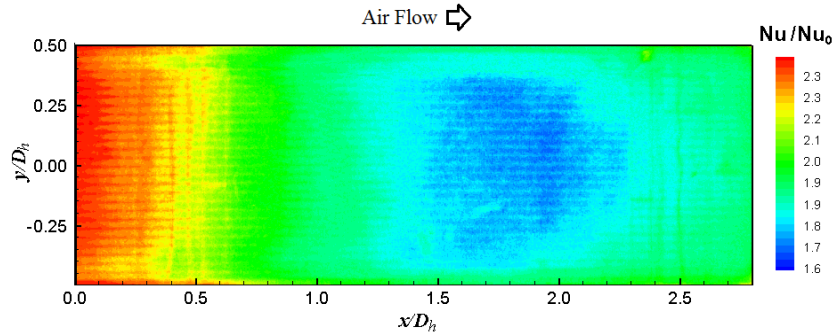

Fig. 3.11 Normalized Nusselt number distributions on the smooth outer wall, Re = 20,000.

The highly enhanced heat transfer $Nu/Nu_0 > 2.2$ is clearly evident in the region $x/D_h <$ 0.3 at the inlet side of the outer wall. This is attributed to the thin boundary layer caused by impingement flow that enters the turn section through the straight inlet channel. The turbulent kinetic energy is somewhat quenched at this impingement zone, which was shown in the PIV measurements of Son et al. [48]. In the region $0.3 < x/D_h$ < 2.0, the impinging flow is then deflected by the outer wall and a wall jet is formed. Due to the strong flow separation and recirculation zone near the inner wall, the cross section of the mainstream becomes smaller and thus leads to flow acceleration, as seen in the simulations by Sundén and Salameh [83] with an identical U-bend geometry. However, with the growing thickness of the wall jet boundary layer, heat transfer drops gradually until a local minimum value $Nu/Nu_0 = 1.7$ is reached at x/D_h = 1.9. Further downstream ($x/D_h > 2.0$), the mainstream begins to turn into the outlet channel and decelerates as the main flow cross section increases, whereas an obvious increase in heat transfer is observed. Wang et al. [73] pointed out that the increased heat transfer enhancement can be explained by the higher turbulence level in the wall jet boundary layer, compared with that upstream but near the impingement region.

It is well known that in the turn region of the sharp U-bend channel, the counter rotating Dean vortex pair appears due to the imbalance of centrifugal force and radial pressure gradients. LDV measurements by Liou [45] revealed that the cross-stream mean velocity of this secondary flow decreases quickly with increasing divider wall length. In this case, the divider wall (or inner wall in the turn region) length is 2.8 D_h, which is larger than in most of the previous studies. Therefore, the influence of the Dean vortex pair on heat transfer of the smooth outer wall might be quite small.

Ribs are often used in heat exchanger systems to enhance heat transfer rates. Figure 3.12 displays the heat transfer distributions on the outer wall with transverse ribs (or 90º ribs) at Re = 20,000. The black color represents the location of the ribs. Note that

the color legend of heat transfer here is different from the previous one on the smooth outer wall.
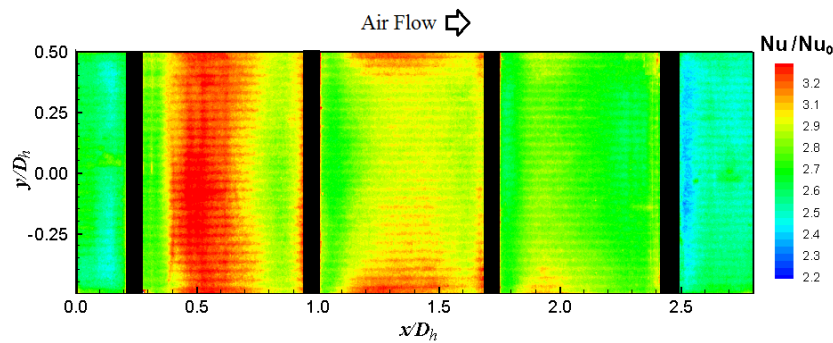

Fig. 3.12 Normalized Nusselt number distributions on the outer wall with 90º ribs, Re = 20,000.

Compared with Fig. 3.11, the presence of ribs further enhances the heat transfer. It is found that the heat transfer distributions are markedly different. The heat transfer does not attain a maximum in the impingement region (x/D_h < 0.3). Smoke visualizations of impingement flow structures along the ribbed wall were performed by Gau and Lee [84]. It appears that close to the stagnation point, the pressure inside the rib-bounded cavity is higher than outside and a recirculating air region is formed enclosing the cavity that prevents the jet flow from penetrating directly. The flow accelerates as it moves away from the impingement region, and the pressure inside the cavity decreases. Heat transfer is very low immediately behind the ribs due to the presence of a flow separation zone there. The separated main flow then reattaches on the outer wall surface (0.4 < x/D_h < 0.8), enhancing the heat transfer significantly (Nu/Nu_0 > 3.0). Further downstream (x/D_h > 1.5), the speed of the reattaching flow decreases because of mainstream deceleration and turning, and a slow reduction of the heat transfer between adjacent ribs is noticed. Due to the fact that the boundary layer on the outer wall is strongly disturbed and the turbulence levels are greatly intensified upstream, the increase of heat transfer downstream, which appears on smooth outer wall, does not show up here. Spanwise variations of the heat transfer levels are as small as those of the smooth outer wall because the transverse ribs mainly generate two dimensional secondary flows.
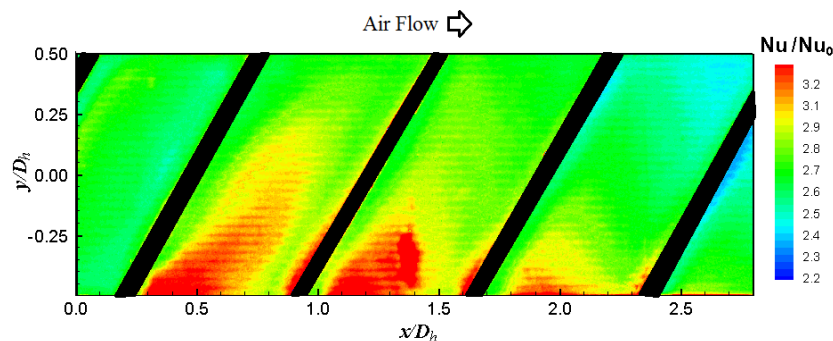

Fig. 3.13 Normalized Nusselt number distributions on the outer wall with 60º ribs, Re = 20,000.

Figure 3.13 displays the heat transfer distributions on the outer wall with 60º angled ribs at Re = 20,000. Similar to that of transverse ribs, the value of Nu/Nu_0 does not peak in the impingement region ($x/D_h < 0.3$) due to the presence of the recirculating air region inside. When ribs are oblique to the mainstream, i.e., the rib has a partial streamwise direction, the flow is driven from the bottom towards the top on the outer wall by the ribs, and returns along the opposite direction above the ribs to close the circulation loop. Due to this secondary flow, the separated region immediately downstream the rib along the bottom wall ($y/D_h < -0.25$) is smaller than that behind the transverse rib. The reattachment of the flow on the bottom of the outer wall is stronger, resulting in higher heat transfer ($Nu/Nu_0 > 3.2$) and higher thermal gradients near the bottom wall. Apart from the reattachment region, another peak of heat transfer is found just upstream the ribs. As the secondary flow moves along the rib from the bottom wall towards the top wall, the separated region and reattachment region increase in size, with a lower impinging velocity of the reattached flow. This leads to reduced heat transfer enhancement and thermal gradients near the top wall, as shown in Fig. 3.13. Further downstream along the main flow direction, a gradual decline of heat transfer from rib to rib is observed. This trend is similar to the case of transverse ribs. Spanwise variations of heat transfer levels are much bigger because of the strong secondary flows generated by the inclined ribs.
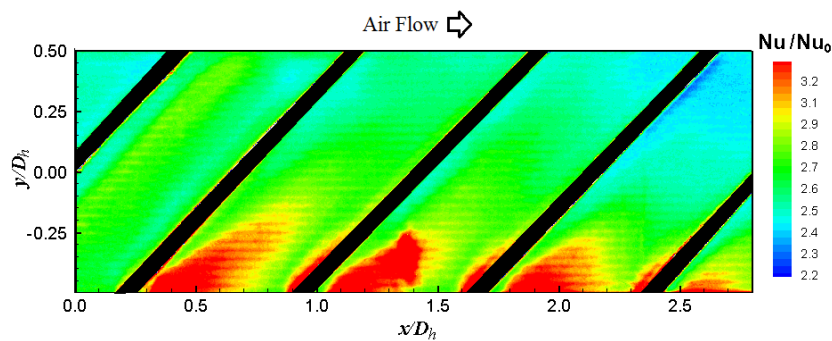
Fig. 3.14 Normalized Nusselt number distributions on the outer wall with 45º ribs, Re = 20,000.

Figure 3.14 illustrates the heat transfer distributions on the outer wall with 45º angled ribs at Re = 20,000. These look similarly to those of 60º angled ribs. However, the effects of secondary flow induced by 45º angled ribs are stronger, leading to even higher heat transfer in a small area near the bottom wall, and lower heat transfer near the top wall. Therefore, larger variations of heat transfer levels appear, both in the spanwise and streamwise directions.
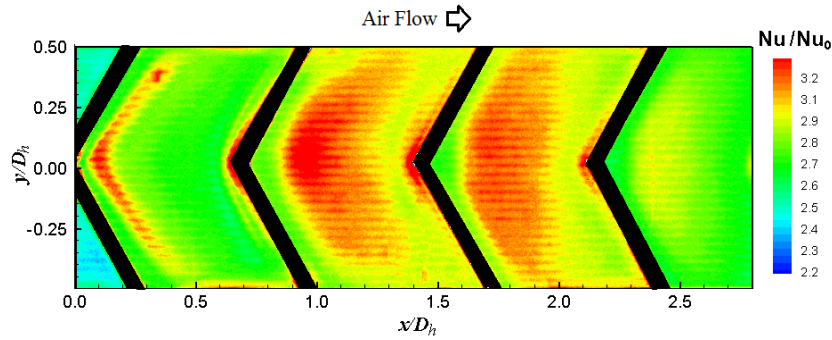
Fig. 3.15 Normalized Nusselt number distributions on the outer wall with 60º V-shaped-upstream ribs, Re = 20,000.

Figure 3.15 displays the heat transfer distributions on the outer wall with 60º V-shaped ribs with the tip facing upstream (60º V-shaped-upstream ribs) at Re = 20,000. The local minimum heat transfer region is observed upstream the first rib. This is due to the separated air region, as explained earlier. The narrow low heat transfer area immediately behind the 60º V-shaped-upstream rib is again due to flow separation, followed by high heat transfer in the flow reattachment region. Each angle side of the V-shaped-upstream rib induces a secondary flow that goes from the midplane to the top or bottom wall on the outer wall, and then returns along the opposite direction. With the mainstream accelerating downstream, this secondary flow is also growing stronger. Between x/D_h = 0.8 and 2.2, the merge of downward washes of these two counterrotating vortices in the midplane region (-0.25 < y/D_h < 0.25) is responsible for the large area of high heat transfer augmentation. Another small area of high heat transfer level is found right upstream every rib. Further downstream, the heat transfer enhancement is weak behind the last rib, which is attributed to the fast decaying of secondary flow by mainstream deceleration and turning.

Fig. 3.16 Normalized Nusselt number distributions on the outer wall with 45º V-shaped-upstream ribs, Re = 20,000.

Figure 3.16 illustrates the heat transfer distributions on the outer wall with 45º V-shaped-upstream ribs at Re = 20,000. Qualitatively, the distributions resemble with that of 60º V-shaped-upstream ribs. However, the areas of high heat transfer enhancement downstream of the ribs seem to be slightly smaller. The peak values of heat transfer at the midline are much larger, which results in higher heat transfer variations in both the streamwise and spanwise directions.

Fig. 3.17 Normalized Nusselt number distributions on the outer wall with 60º V-shaped-downstream ribs, Re = 20,000.

Figure 3.17 displays the heat transfer distributions on the outer wall with 60º V-shaped ribs with the tip facing downstream (60º V-shaped-downstream ribs) at Re = 20,000. Again in the region $x/D_h < 0.3$ at the inlet side of the outer wall, the low heat transfer is caused by the separated air region. Separation behind ribs reduces the heat transfer levels. The two counterrotating vortices induced by each angled side of the V-shaped-downstream ribs are in opposite directions with those induced by V-shaped-upstream ribs, which result in the completely different heat transfer distributions. The high heat transfer areas in this case are located in the regions adjacent to the top ($y/D_h > 0.3$) and bottom ($y/D_h < -0.3$) walls, where the velocities of the rib-induced secondary flow are directed towards the outer wall surface. In the middle part of the outer wall where the secondary flow is directed away from the bottom wall (-0.2 < $y/D_h < 0.2$), heat transfer is low.
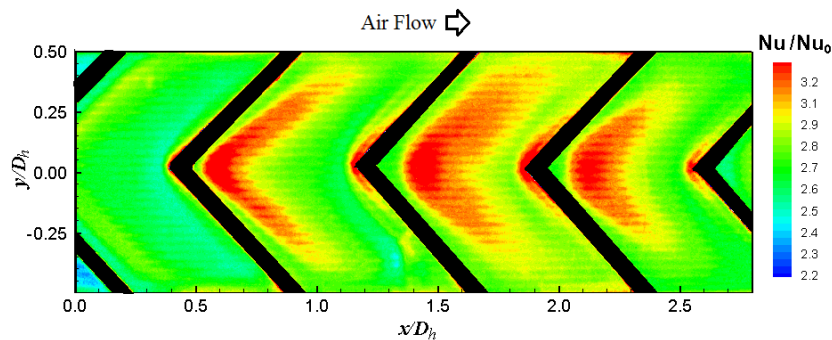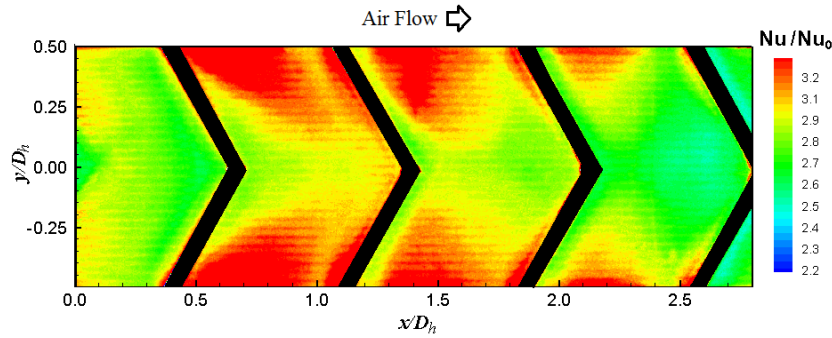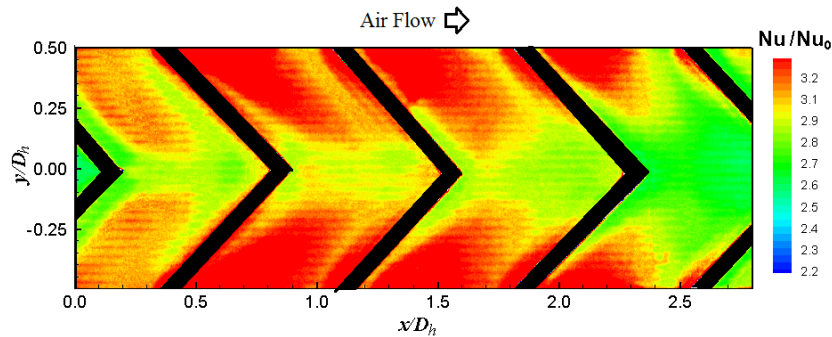

Fig. 3.18 Normalized Nusselt number distributions on the outer wall with 45º V-shaped-downstream ribs, Re = 20,000.

Figure 3.18 illustrates the heat transfer distributions on the outer wall with 45º V-shaped-downstream ribs at Re = 20,000. Basically the distributions are similar to those of 60º V-shaped-downstream ribs. However, the downward wash of the secondary flow induced by 45º V-shaped-downstream ribs is slightly stronger than that by 60º V-shaped-downstream ribs. Therefore, Fig. 3.18 presents a slightly smaller low-heat-transfer region immediately downstream of each rib. Moreover, there are larger high-heat-transfer areas close to the top ($y/D_h > 0.2$) and bottom ($y/D_h < -0.2$) walls.

3.2.3 Average heat transfer and pressure drop

Figure 3.19 depicts the area-averaged Nusselt number ratio and friction factor ratio for smooth and ribbed outer walls, at Re = 20,000, and 26,000. The results show that the heat transfer enhancement magnitude can decrease as the Reynolds number increases, while the friction factor ratio increases with increasing Reynolds number, both for the smooth and ribbed outer wall, as previously shown in studies of different rib configurations in a straight channel [59-64].

Fig. 3.19 Area-averaged Nusselt number ratio and average friction factor ratio for smooth and ribbed outer walls, Re = 20,000, and 26,000.

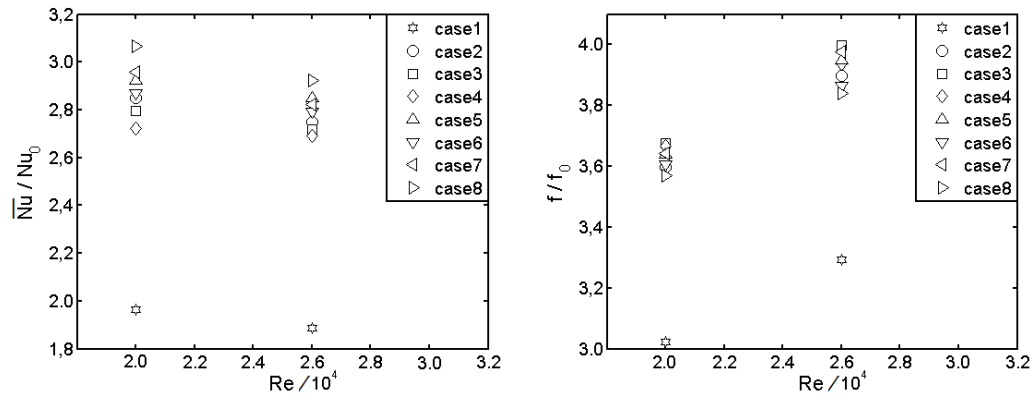For the smooth outer wall, the heat transfer is enhanced by a factor of 1.8 to 2.0 while the pressure drop increases 3.0 to 3.3 times. Ribs improve the heat transfer ($2.6 < \overline{Nu} / Nu_0 < 3.2$) with an increased pressure drop penalty ($3.5 < f/f_0 < 4.0$). For all the rib configurations studied, 45º V-shaped-downstream ribs provide the highest Nusselt number ratio with a low friction factor ratio. This is probably due to the favorable interaction between secondary flows induced by ribs and the Dean vortex pair. The 60º V-shaped-downstream and 60º V-shaped-upstream ribs give almost the same heat transfer enhancement and pressure drop increment. Both of them are slightly higher than those of the 45º V-shaped-upstream rib. Note that 45º angled ribs have the lowest Nusselt number ratio, even lower than for the 60º and 90º angled ribs.

3.2.4 Thermal performance and heat transfer non-uniformity

Figure 3.20 presents the thermal performance and heat transfer non-uniformity for the smooth and ribbed outer walls, at Re=20,000, and 26,000, respectively. $\eta = (\overline{Nu} / Nu_0) / (f / f_0)^{1/3}$ is used to evaluate the thermal performance based on the same heat transfer surface area and pumping power. The standard deviations of the normalized Nusselt number distributions $(Nu/Nu_0)_{std}$ on the outer wall with and without ribs are calculated to examine the heat transfer non-uniformity. Large deviation represents high non-uniformity of heat transfer. For all the cases studied, it is found that with increasing Reynolds number, the thermal performance decreases while the heat transfer non-uniformity is kept almost constant.
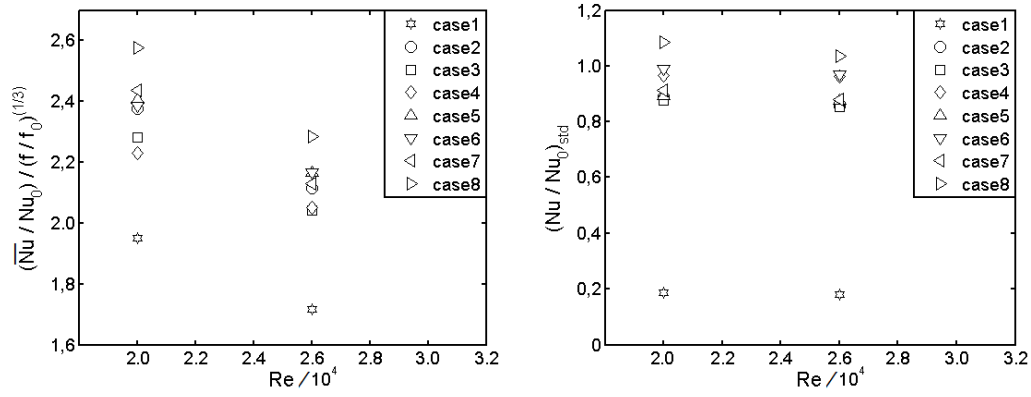
Fig. 3.20 Thermal performance and heat transfer non-uniformity for smooth and ribbed outer walls, Re = 20,000, and 26,000.

The smooth bend shows the lowest thermal performance ($1.6 < \eta < 2.0$) and heat transfer non-uniformity ($0.15 < (Nu/Nu_0)_{std} < 0.25$). Among all the rib configurations tested, 45º V-shaped-downstream ribs exhibit best thermal performance ($2.2 < \eta < 2.6$), at the cost of the highest heat transfer non-uniformity ($1.0 < (Nu/Nu_0)_{std} < 1.1$). Moreover, all the three 45º (V-shaped-downstream, V-shaped-upstream and angled) ribs give higher heat transfer non-uniformity than other ribs, which is because of stronger 3D secondary flows induced by 45º ribs. The 60º V-shaped-downstream and V-shaped-upstream ribs provide slightly lower thermal performances than the 45º V-shaped-downstream rib, while they give more uniform heat transfer distributions. The lowest thermal performance is obtained by 45º angled ribs.

4 Conclusions and future work

The work presented in this thesis can be summarized as follows:

(1) Experimental investigations of the heat transfer characteristics of an OGV in a linear cascade have been conducted. Liquid crystal thermography was calibrated for various viewing angles and used to measure the wall temperature. Both the on- and off-design conditions were tested. Results indicated that the effect of Reynolds number is to increase the magnitude of heat transfer coefficient but without changing the heat transfer patterns. On the other hand, the change of incidence angle had a significant impact on the heat transfer. It is found that the stagnation point moved from the pressure side to the suction side when the incident angle was changed from +25 degrees to -25 degrees. Moreover, the onset of flow transition on the suction side was shifted downstream. The heat transfer on the pressure side exhibited different trends at different incidence angles. For the on-design condition (+25 degrees), the local heat transfer valley was followed by a plateau; for the off-design condition (-25 degrees). However, the heat transfer exhibited a sharp decrease which was followed by a gradual increase until the trailing edge.

The endwall heat transfer characteristics of an OGV in a linear cascade have also been investigated. Both the on- and off-design conditions were tested. It was found that the endwall heat transfer coefficients for off-design conditions are generally higher than those for on-design condition. The results indicate that the incidence angle of OGVs has a significant effect on the endwall heat transfer.

(2) Experiments of detailed heat transfer and pressure drop distributions were carried out in the smooth and ribbed turn region of a U-bend internal cooling channel related to gas turbine blades.

Upstream the turn, the local pressure drops linearly. Just after the turn, the pressure decreases quickly to a minimum and then recovers due to the turn-induced separation. The ribs on the outer wall cause a relatively larger pressure drop over the turn region compared to the smooth case.

For the smooth outer wall in the turn region, the local heat transfer is dominated by the impingement. For the ribbed outer wall in the turn region, no rib-related heat transfer augmentation is found at the impingement region. As the mainstream accelerates and flow reattaches on the outer wall surface, heat transfer in the middle part is enhanced significantly.

The area-averaged heat transfer on the smooth outer wall is enhanced 1.8 to 2.0 times, at the penalty of 3.0 to 3.3 times pressure loss. The presence of ribs augments the heat transfer by about 2.6 to 3.2 times on the outer wall. Pressure drop penalty also increases 3.5 to 4.0 times.

Thermal performance and heat transfer non-uniformity were evaluated. Among all the rib configurations studied, the 45º V-shaped-downstream ribs

give the best thermal performance. However, the 60º V-shaped-downstream and V-shaped-upstream ribs provide much more uniform heat transfer distributions.

For the future work:

(1) A fillet will be put on the edge of OGV. It is of interest to study the effects of fillet on the endwall heat transfer.

Flow measurements in the linear cascade with OGV are needed to have a better understanding of the convective heat transfer behavior.

Numerical simulations can be made and compared with the experimental data.

(2) Investigate the effects of film cooling holes on the heat transfer in the turn region with ribs.

Study the impingement cooling in cross-flow modified by ribs.

5 References

[1]   Han J. C., Datta S., and Ekkad S., 2012, "Gas turbine heat transfer and cooling technology", CRC Press.

[2]   Goldstein R. J., 2001, "Heat transfer in gas turbine systems", Annals of the New York Academy of Sciences, 934, pp: xi-xii.

[3]   Sundén B., and Faghri M., 2001, "Heat transfer in gas turbine", WIT, Southampton, UK.

[4]   Sundén B., and Xie G., 2010, "Gas turbine blade tip heat transfer and cooling: a literature survey", Heat Transfer Engineering, 31(7), pp: 527-554.

[5]   Bunker R. S., 2001, "A review of turbine blade tip heat transfer", Annals of the New York Academy of Sciences, 934, pp: 64-79.

[6]   Koch H., Hoeger M., and Kozulovic D., 2012, "Outlet guide vane for low pressure turbine configurations". In 42nd AIAA Fluid Dynamics Conference and Exhibit, pp: 1564-1573.

[7]   Dahlström S., 2000, "Large eddy simulation of the flow around a high-lift airfoil", PhD thesis, Chalmers University of Technology, Göteborg, Sweden.

[8]   Nealy D. A., Mihelc M. S., Hylton L. D., and Gladden H. J., 1984, "Measurements of heat transfer distribution over the surfaces of highly loaded turbine nozzle guide vane", ASME Journal of Engineering for Gas Turbines and Power, 106, pp: 149-158.

[9]   Ames F. E., 1997, "The influence of large-scale high-intensity turbulence on vane heat transfer", ASME J. Turbomach., 119, pp: 23-30.

[10]   Ames F. E., Wang C., and Barbot P. A., 2003, "Measurement and prediction of the influence of catalytic and dry low NOx combustor turbulence on vane surface heat transfer", ASME J. Turbomach., 125, pp: 210-220.

[11]   Arts T., Lambert de Rouvroi M., and Rutherford A. W., 1990, "Aero-thermal investigation of a highly loaded transonic linear turbine guide vane cascade", Von Karman Institute for Fluid Dynamics, Technical Note 174.

[12]   Stripf M., Schulz A., and Wittig S., 2005, "Surface roughness effects on external heat transfer of a HP turbine vane", ASME J. Turbomach., 127, pp: 200-208.

[13]   Liu X., and Rodi W., 1994, "Surface pressure and heat transfer measurements in a turbine cascade with unsteady oncoming wakes", Experiments in Fluids, 17, pp: 171-178.

[14]   Wissink J., and Rodi W., 2006, "Direct numerical simulation of flow and heat transfer in a turbine cascade with oncoming wakes", Journal of Fluid Mechanics, 569, pp: 209-247.

[15]   Rhee D. H, and Cho H. H, 2008, "Effect of vane/blade relative position on heat transfer characteristics in a stationary turbine blade: Part 2 Blade surface",

International Journal of Thermal Sciences, 47, pp: 1544-1554.

[16] Blair M. F., Dring R. P., and Joslyn H. D., 1989, "The effects of turbulence and stator/rotor interactions on turbine heat transfer: Part I-design operating conditions", ASME J. Turbomach., 111, pp: 87-96.

[17] Blair M. F., Dring R. P., and Joslyn H. D., 1989, "The effects of turbulence and stator/rotor interactions on turbine heat transfer: Part II-effects of Reynolds number and incidence", ASME J. Turbomach., 111, pp: 97-103.

[18] Ames F. E., Peters J. M., and Crook B. A., 2010, "Effects of incidence angle on the performance of lightly loaded turbine guide vanes", In 48th AIAA Aerospace Sciences Meeting Including the New Horizons Forum and Aerospace Exposition Orlando, USA, AIAA 2010-408.

[19] Simon F., 1993, "A research program for improving heat transfer prediction for the laminar to turbulent transition region of turbine vanes/blades", NASA Technical Memorandum 106278.

[20] Gaugler R. E., 1985, "A review and analysis of boundary layer transition data for turbine application", NASA Technical Memorandum 86880.

[21] Meschwitz S., 1991, "The effect of angle of incidence and Reynolds number on heat transfer in a linear turbine cascade", PhD thesis, Air Force Institute of Technology, Air University, USA.

[22] Consigny H., and Richards B. E., 1982, "Short duration measurements of heat transfer rate to a gas turbine rotor blade", ASME Journal of Engineering for Gas Turbines and Power, 104, pp: 542-551.

[23] Hippensteele S. A., Russell L. M., and Torres F. J., 1985, "Local heat-transfer measurements on a large scale-model turbine blade airfoil using a composite of a heater element and liquid crystals", ASME Journal of Engineering for Gas Turbines and Power, 107, pp: 953-960.

[24] Hjärne J., 2007, "Turbine outlet guide vane flows", PhD thesis, Chalmers University of Technology, Göteborg, Sweden.

[25] Chernoray V., Larsson J., and Ore S., 2010, "Effect of geometry deviations on the aerodynamic performance of an outlet guide vane cascade", In ASME Turbo Expo 2010: Power for Land, Sea and Air, Glasgow, UK, ASME paper GT2010-22923.

[26] Lalit H., and Chernoray V., 2010, "Experimental study of the influence of surface non-conformances on the low pressure turbine outlet guide vane flow", In 27th International Congress of the Aeronautical Sciences, Nice, France.

[27] Langston L. S., Nice M. L., and Hooper R. M., 1977, "Three-dimensional flow within a turbine cascade passage", ASME Journal of Engineering for Gas Turbines and Power, 99(1), pp: 21-28.

[28] Graziani R. A., Blair M. F., Taylor J. R., and Mayle R. E., 1980, "An experimental study of endwall and airfoil surface heat transfer in a large scale turbine blade cascade", ASME Journal of Engineering for Gas Turbines and Power, 102(2), pp: 257-267.

[29] Sjolander S. A., 1975, "The endwall boundary layer in an annular cascade of turbine nozzle guide vanes", Carleton University, Department of Mechanical

and Aeronantal Engineering, Ottawa, Canada, TR ME/A 75–4.

[30] Langston L. S., Nice M. L., and Hooper R. M., 1976, "Three-dimensional flow within a turbine cascade passage", ASME Paper No. 76-GT-50.

[31] Sharma O. P., and Butler T. L., 1987, "Predictions of endwall losses and secondary flows in axial flow turbine cascades", ASME J. Turbomach., 109, pp: 229–236.

[32] Blair M. F., 1974, "An experimental study of heat transfer and film cooling on large-scale turbine endwalls", ASME J. Heat Transfer, 96, pp: 524–529.

[33] Hippensteele S. A., and Russell L. M., 1988, "High resolution liquid-crystal heat-transfer measurements on the endwall of a turbine passage with variations in Reynolds number", NASA Technical Memorandum 100827.

[34] Giel P. W., Thurman D. R., VanFossen G. J., Hippensteele S. A., and Boyle R. J., 1998, "Endwall heat transfer measurements in a transonic turbine cascade", ASME J. Turbomach., 120, pp: 305–313.

[35] Kang M., Kohli A., and Thole K. A., 1999, "Heat transfer and flow field measurements in the leading edge region of a sator vane endwall", ASME J. Turbomach., 121, pp: 558–568.

[36] Harvey N. W., and Jones T. V. 1990, "Measurement and calculation of end wall heat transfer and aerodynamics on a nozzle guide vane in annular cascade", In ASME, 35th International Gas Turbine and Aeroengine Congress and Exposition.

[37] Nicklas M., 2001, "Film-cooled turbine endwall in a transonic flow field: part II—heat transfer and film-cooling effectiveness", ASME J. Turbomach., 123(4), pp: 720-729.

[38] Wang L., Sundén B., Chernoray V., and Abrahamsson H., 2012, "Experimental study of endwall heat transfer in a linear cascade", Journal of Physics: Conference Series, 395, 012028.

[39] Wang L., Sundén B., Chernoray V., and Abrahamsson H., 2013, "Endwall heat transfer measurements of an outlet guide vane at on and off design conditions", In ASME Turbo Expo 2013: Power for Land, Sea and Air, Texas, USA, ASME paper GT2013-95008.

[40] Metzger D. E., Plevich C. W., and Fan C. S., 1984, "Pressure loss through sharp 180 deg turns in smooth rectangular channels", ASME Journal of Engineering for Gas Turbines and Power, 106, pp: 677–681.

[41] Fan C. S., and Metzger D. E., 1987, "Effect of channel aspect ratio on heat transfer in rectangular passage sharp 180-deg turns", 32nd International Gas Turbine Conference and Exhibition, 87-GT- 113.

[42] Metzger D., and Sahm M., 1986, "Heat transfer around sharp 180-deg turns in smooth rectangular channels", ASME J. Heat Transfer, 108, pp: 500–506.

[43] Metzger D. E., Fan C. S., and Plevich C. W., 1988, "Effects of transverse rib roughness on heat transfer and pressure losses in rectangular ducts with sharp 180 degree turns", AIAA Paper No. 88-0166.

[44] Wang T. S., and Chyu M. K., 1994, "Heat convection in a 180-deg turning duct with different turn configurations", AIAA J. Thermophys. Heat Transfer, 8, pp:

595-601.

[45] Liou T. M., Tzeng Y. Y., and Chen C. C., 1999, "Fluid flow in a 180 deg sharp turning duct with different divider thickness", ASME J. Turbomach., 121, pp: 569-576.

[46] Liou T. M., Chen C. C., Tzeng Y. Y., and Tsai T. W., 2000, "Non-intrusive measurements of near-wall fluid flow and surface heat transfer in a serpentine passage", Int. J. Heat Mass Transfer, 43, pp: 3233-3244.

[47] Ekkad S. V., and Han J. C., 1997, "Detailed heat transfer distributions in two-pass square channels with rib turbulators", Int. J. Heat Mass Transfer, 40, pp: 2525-2537.

[48] Son S.Y., Kihm K.D., and Han J.C., 2002, "PIV flow measurements for heat transfer characterization in two-pass square channels with smooth and 90° ribbed walls", Int. J. Heat Mass Transfer, 45, pp: 4809-4822.

[49] Hirota M., Fujita H., Syuhada A., Araki S., Yoshida, T., and Tanaka, T., 1999, "Heat/mass transfer characteristics in two-pass smooth channels with a sharp 180-deg turn", Int. J. Heat Mass Transfer, 42, pp: 3757-3770.

[50] Nakayama H., Hirota M., Fujita H., Yamada T., and Koide Y., 2006, "Fluid flow and heat transfer in two-pass smooth rectangular channels with different turn clearances", ASME J. Turbomach., 128, pp: 772-785.

[51] Chang S. W., and Cai Z. X., 2008, "Heat transfer and pressure drop in two-pass rib-roughened square channels with bleed from sharp bend", Int. J. Heat Fluid Flow, 31, pp: 19-31.

[52] Jenkins S. C., Zehnder F., Shevchuk I. V., von Wolfersdorf J., Weigand, B., and Schnieder, M., 2013, "The effects of ribs and tip wall distance on heat transfer for a varying aspect ratio two-pass ribbed internal cooling channel", ASME J. Turbomach., 135, 021001.

[53] Siddique W., EI-Gabry L., Shevchuk I. V., Hushmandi N. B., and Fransson, T. H., 2012, "Flow structure, heat transfer and pressure drop in varying aspect ratio two-pass rectangular smooth channels", Heat Mass Transfer, 48, pp: 735-748.

[54] Siddique W., Shevchuk I. V., EI-Gabry L., Hushmandi N. B., and Fransson T. H., 2013, "On flow structure, heat transfer and pressure drop in varying aspect ratio two-pass rectangular channel with ribs at 45°", Heat Mass Transfer, 49, pp: 679-694.

[55] Schüler M., Zahnder F., Weigand B., von Wolfersdorf J., and Neumann S. O., 2011, "The effect of turning vanes on pressure loss and heat transfer of a ribbed rectangular two-pass internal cooling channel", ASME J. Turbomach., 133, 021017.

[56] Saha K., and Acharya S., 2013, "Effect of bend geometry on heat transfer and pressure drop in a two-pass coolant square channel for a turbine", ASME J. Turbomach., 135, 021035.

[57] Verstraete T., Coletti F., Bulle J., Vanderwielen T., and Arts T., 2013, "Optimization of a U-Bend for minimal pressure loss in internal cooling channels-Part I: Numerical menthod", ASME J. Turbomach., 135, 051015.

[58] Coletti F., Verstraete T., Bulle J., Wielen T., Berge N., and Arts T., 2013, "Optimization of a U-Bend for minimal pressure loss in internal cooling channels-Part II: Experimental validation", ASME J. Turbomach., 135, 051016.

[59] Han J. C., 1984, "Heat transfer and friction in channels with two opposite rib-roughened walls", ASME J. Heat Transfer, 106(4), pp: 774-781.

[60] Han J. C., 1988, "Heat transfer and friction characteristics in rectangular channels with rib turbulators", ASME J. Heat Transfer, 110(2), pp: 321-328.

[61] Han J. C., Zhang Y. M., and Lee C. P., 1991, "Augmented heat transfer in square channels with parallel, crossed, and V-shaped angled ribs", ASME J. Heat Transfer, 113, pp: 590-596.

[62] Han J. C., and Zhang Y. M., 1992, "High performance heat transfer ducts with parallel broken and V-shaped broken ribs", Int. J. Heat Mass Transfer, 35(2), pp: 513-523.

[63] Tanda G., 2004, "Heat transfer in rectangular channels with transverse and V-shaped broken ribs", Int. J. Heat Mass Transfer, 47(2), pp: 229-243.

[64] Chandra P. R., and Han J. C., 1989, "Pressure drop and mass transfer in two-pass ribbed channels", AIAA J. Thermophys. Heat Transfer, 3(3), pp: 315-320.

[65] Mochizuki S., Murata A., Shibata R., and Yang W. J., 1999, "Detailed measurements of local heat transfer coefficients in turbulent flow through smooth and rib-roughened serpentine passages with a 180 sharp bend", Int. J. Heat Mass Transfer, 42(11), pp: 1925-1934.

[66] Ekkad S. V., Huang Y., Han J. C., 1998, "Detailed heat transfer distributions in two-pass square channels with rib turbulators and bleed holes", Int. J. Heat Mass Transfer, 41(23), pp: 3781-3791.

[67] Bunker R. S., 2008, "The augmentation of internal blade tip-cap cooling by arrays of shaped pins", ASME J. Turbomach., 130, 041007.

[68] Xie G. and Sundén B., 2011, "Conjugated analysis of heat transfer enhancement of an internal blade tip-wall with pin-fin arrays", J. Enhanced Heat Transfer, 18, pp: 149-165.

[69] Xie G. and Sundén B., 2010, "Numerical predictions of augmented heat transfer of an internal blade tip-wall by hemispherical dimples", Int. J. Heat Mass Transfer, 53, pp: 5639-5650.

[70] Salameh T. and Sundén B., 2010, "An experimental study of heat transfer and pressure drop on the bend surface of a U-duct", Proceedings of the 2010 ASME Turbo Expo, GT2010-22139.

[71] Salameh T. and Sundén B., 2011, "Effects of ribs on internal blade-tip cooling", Proceedings of the 2011 ASME Turbo Expo, GT2011-45118.

[72] Wang L., Ghorbani-Tari Z., Wang C., and Sundén B., 2013, "An experimental study of Heat transfer in a U-bend duct with and without ribs", 8th World Conference on Experimental Heat Transfer, Fluid Mechanics, and Thermodynamics.

[73] Wang L., Ghorbani-Tari Z., Wang C., and Sundén B., 2013, "Heat transfer on a ribbed U-bend relevant for the blade-tip cooling", 2nd International Workshop

on Heat Transfer Advances for Energy Conservation and Pollution Control, IWHT2013-010.

[74] Tschierske C., 1988, "Non-conventional liquid crystals—the importance of micro-segregation for self-organisation", Journal of Materials Chemistry 8(7) pp: 1485-1508.

[75] Jones T. V., 1992, "The use of liquid crystals in aerodynamic and heat transfer testing", Proc. 4th Int. Symp. on Transport Phenomena in Heat and Mass Transfer, 2, pp: 1242–1273.

[76] Gao X., 2002, "Heat transfer and fluid flow investigation in ribbed ducts and impinging jets using liquid crystal thermography and PIV", PhD thesis, Department of Energy Sciences, Lund University, Sweden.

[77] Wang, L., 2007. "Experimental studies of separated flow and heat transfer in a ribbed channel", PhD thesis, Department of Energy Sciences, Lund University, Sweden.

[78] Moffat R. J., 1998, "Describing the uncertainties in experimental results", Experimental Thermal and Fluid Sciences, 1, pp: 3-17.

[79] Dittus P. W., and Boelter L. M. K., 1985, "Heat transfer in automobile radiators of the tubular type", Int. Comm. Heat Mass Transfer, 12, pp: 3-22.

[80] Webb R. L., and Kim N. H., 1994, "Principles of enhanced heat transfer", Wiley, New York.

[81] Wang T., 1984, "Experimental investigation of curvature and free-stream turbulence effects on heat transfer and fluid mechanics in transitional boundary layers", PhD thesis, Department of Mechanical Engineers, University of Minnesota, USA.

[82] Kim J., and Simon T. W., 1991, "Free-stream turbulence and concave curvature effects on heated, transitional boundary layers", NASA CR-187150.

[83] Sundén B., and Salameh T., 2013, "A numerical investigation of heat transfer in a smooth bend part of a u-duct", International Journal of Numerical Methods for Heat & Fluid Flow, 24(1), pp: 9-9.

[84] Gau C., and Lee C. C., 1992, "Impingement cooling flow structure and heat transfer along rib-roughened walls", Int. J. Heat Mass Transfer, 35(11), pp: 3009-3020.